The Effect of Approximating a Temperature-Dependent Specific Heat in Enthalpic Lattice Boltzmann Method Phase Change Heat Transfer Simulations

TN2983: Bachelor Thesis

Midas van Winden

Delft University of Technology

TUDelft

The Effect of Approximating a Temperature-Dependent Specific Heat in Enthalpic Lattice Boltzman Method Phase Change Heat Transfer Simulations

TN2983: Bachelor Thesis

by

Midas van Winden

to obtain the degree of Bachelor of Science

at the Delft University of Technology,

to be defended on Monday July 14, 2025 at 14:15.

TUDelft

Highlights

- Multiple enthalpic lattice Boltzmann method-based models were developed to simulate heat transfer in phase-changing materials, in which the temperature profile over distance and the melting/freezing front propagation over time for certain parameters are determined.

- The investigated cases uniformly support the conclusion that the relative error of assuming a temperature-independent specific heat is limited

- The models which, theoretically, reasonability approached physical reality were successfully benchmarked against analytical solutions and experimental measurements, when the additional heat conduction paths and heat losses are taken into account.

Abstract

In the transition towards a carbon-neutral energy supply, Molten Salt Fast Reactors (MSFR) present a promising alternative to conventional nuclear reactors. In the electricity generation, heat transfer plays an essential role. Accurate modeling of this is important for the safe and efficient operation of such systems. A widely used approach to model heat transfer problems is the enthalpic lattice Boltzmann method (HLBM). A common assumption in this method is the use of a temperature-independent specific heat as an assumption to model materials with a temperature-dependent specific heat.

In this thesis, the consequence of this assumption on the outcome of enthalpic LBM-based models is investigated, specifically for cases where a phase transition occurs. Furthermore, multiple enthalpic LBM schemes are proposed in order to accurately, simply and in a computationally efficient manner incorporate the temperature-dependent specific heat into the enthalpic lattice Boltzmann method.

Three benchmarked cases were studied, involving freezing problems in water and melting problems in paraffin. The results show that the relative error introduced by assuming a temperature-independent specific heat remain relatively low, with a highest found absolute value of 5.4%. This relative error of certain temperature-independent specific heat estimates is not strongly affected by the spatial resolution, but it is increased by an increasing temperature difference between a materials freezing / melting temperature and the intial and wall temperatures.

The study further reveals that certain temperature-independent values for the specific heat in the HLBM can excellently approach the numerical solution of the model based on a temperature-dependent specific heat. Experimental validation of the models for the paraffin melting problem confirmed the enthalpic LBM model's ability to reflect physical reality, provided that heat losses and additional conduction paths are taken into account.

Contents

<div align="right">

1

</div>

<div align="right">

Introduction

</div>

To abide by the Paris Climate Agreement, which was established in 2016 to prevent catastrophic global consequences as a result of climate change, it is of great importance to reduce the amount of mankind-caused CO_2 emissions. Since a large fraction of CO_2 is emitted in electricity generation [3], a carbon-neutral electricity generation system can play a significant role in ensuring the success of the Paris Agreement. Wind, hydro and solar energy are important forms of green energy production in the current efforts of governments to reduce emissions. However, because of natural fluctuations of the output of these energy sources, it is not efficient and energy secure to limit the energy generation of the future solely to these energy sources. A certain base load, independent of the temporal natural circumstances, but still flexible enough to react on the real-time electricity demand would therefore be desirable. The most realistic carbon-free technology to deliver this base load is nuclear energy.

However, in the public domain, there is still a lot of fear about implementing nuclear energy, due to big accidents in the past and the everlasting nuclear waste which is produced while generating nuclear energy. An advanced new form of the conventional Pressurized Water Reactor (PWR) is therefore desirable. One of the possible successors of the PWR is the Molten Salt Fast Reactor (MSFR).

1.1. Molten Salt Fast Reactor

A Molten Salt Fast Reactor (MSFR) uses a liquid mixture of carrier salts and fissile elements as its fuel, which is in the core of the reactor. The fissile elements are often composed of compounds containing uranium and thorium, while the molten salt is composed of enriched lithium fluoride [21]. In the molten salt mixture, nuclear fission of these fissile elements takes place, generating heat, to which the molten salt itself acts as a coolant. The MSFR operates at a temperature of 750°C and under low pressure (often almost atmospheric) [1, 13]. This molten salt then leaves the reactor core and exchanges its heat via a heat exchanger to a secondary coolant, which might be water or a secondary salt. This secondary coolant is then transported to a circuit where its heat is used to generate electricity. [1, 21] An illustration of the reactor core is shown in figure 1.1

A big advantage of the MSFR is that it is very safe. Due to the (liquid) nature of the molten salt fuel mixture, nuclear meltdowns as known from conventional reactors are impossible. In the event of an emergency, the molten salt mixture automatically drops down to dump tanks. Due to the low operating pressure of the fluid, the risk of a system explosion is greatly reduced [13, 21]. Furthermore, the MSFR has the capability to load-follow, in contrast to conventional reactors. This can be done by controlling the water flowrate into the steam generator. This is possible due to the large heat storage capacity and negative temperature feedback of the molten salt fuel mixture [13]. In addition, less nuclear waste is produced and the half-life time of the nuclear waste produced is much shorter than that of conventional reactors [21].

For the safety and efficiency of the MSFR, it is very important to have a thorough understanding of the nature of the heat transfer processes occurring in the MSFR. To gain this understanding, numerical models are used to model the heat transfer among other things. An often used method to numerically
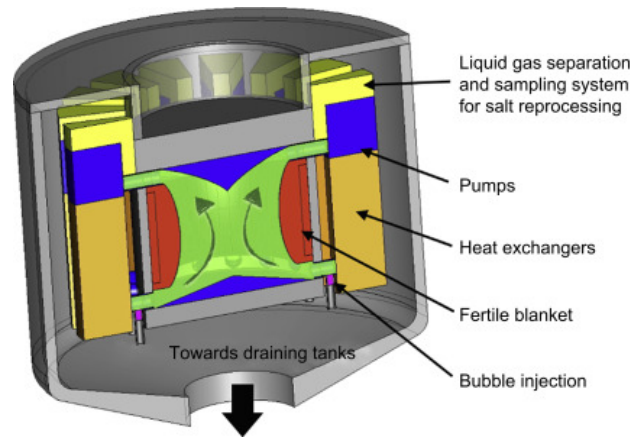
Figure 1.1: Illustration of the reactor core of a Molten Salt Fast Reactor, obtained from Allibert et al. (2016) [1]

assess the heat transfer is the lattice Boltzmann method.

1.2. Lattice Boltzmann Method

The lattice Boltzmann method (LBM) is a numerical method that originates from the Boltzmann equation as its discrete variant. The LBM is often used to simulate situations based on the Navier-Stokes equation or an equation in a similar form, since its most common used form is a second-order accurate solver for the weakly compressible Navier-Stokes equation. It is a method that works on the mesoscopic scale, since it does not consider the behavior of individual particles but rather that of the particle distributions. These particle distributions are tracked in space and time and define the macroscopic properties of the system in space and time. The big advantage of the LBM is that non-linear and non-local calculations are transformed into resp. linear and local problems. This removes some of the numerical complexity of the simulation, since the simulation does not involve i.e. the Poisson equation [20]. Furthermore, this makes the LBM highly parallelisable, which is beneficial for computational performance and makes computing on high-performance parallel architectures such as GPUs possible, making the numerical process faster. [20]

The lattice Boltzmann method can, as said, be extended to solve equations which are similar to the Navier-Stokes equation. This can be done, among others, to numerically assess multi-phase heat transfer flows, which makes this method relevant for this thesis. Wolf-Gladrow (1995) [31] was one of the first to derive a lattice Boltzmann method that could solve diffusion problems, initiating the use of the LBM for heat transfer. Based on this method, thermal LB models for solid–liquid phase change problems were proposed, among which De Fabritiis et al. (1998) [8] had a great impact. This thermal LBM was further developed to an enthalpy-based LBM by Jiaung et al. (2001) [16] to make the LBM suitable for phase change problems [14]. This enthalpic LBM was adapted by many authors to achieve optimal efficiency and align the method with the specific problem to be solved. One of these was Huang et al. (2013) [14], on whose proposed enthalpic LBM the method used in this thesis will be based.

In most researches in which the LBM is used, it is assumed that the thermophysical properties of the materials, such as the specific heat c_p, thermal conductivity λ and density ρ, are constant over temperature. These assumptions are also made in the proposed lattice Boltzmann methods discussed earlier. However, this is not always a reasonable assumption. Few studies have been done on the effect of this on its solutions and on how this can be incorporated in the LBM. Studies conducted have often focused on the effect of a variable thermal conductivity λ [11, 12, 23, 29]. Only one study, Chen et al. (2016) [7], has been found to partly incorporate a variable specific heat c_p. However, in this study, still approximations of a constant c_p are used. To further develop the lattice Boltzmann method to provide reliable and physically correct results for heat transfer problems, the implementation of the lattice Boltzmann method for situations with a variable specific heat c_p needs to be investigated further. Furthermore, the effect of assuming a constant c_p for convenience, when this is not the case, on the solution given by the LBM should be investigated, since this is an often used method by researchers due to the absence of an user-friendly model to incorporate the variance of c_p in the model.

1.3. Thesis Goals and Outline

In this study, the effect of the assumption of a constant specific heat c_p per phase over temperature for multiphase systems, when this is not necessarily the case, in the enthalpic lattice Boltzmann method is investigated. For simplicity, this will be realized in a one dimensional LBM scheme with no convection, but an effort will be made to generalize the results to multiple dimensions. To reach this goal, multiple enthalpic LBM-based schemes with different parameter assumptions are implemented, which can be compared to each other and available analytical solutions of the heat transfer problem. An analysis of the propagation of the melting/freezing front and the temperature profile in the materials researched for the different schemes will be the key points of comparison. In order to accomplish this, multiple new schemes will be proposed in order to find an optimal efficient and accurate enthalpic LBM scheme which incorporates the effect of the variability in c_p in the model, some of which are based on existing literature, and others will follow from the theoretical analysis in this thesis. These new LBM schemes will also be compared to each other in terms of efficiency, simplicity and accuracy. By doing this, it can be concluded if, and under which circumstances, an certain assumption about the specific heat can be made. To validate the new proposed LBM schemes, an experiment, in which the behavior of heated paraffin is studied, will be conducted. These results will be compared to the model in an effort to draw conclusions about to what extent the newly proposed models reflect reality.

1.3.1. Research Questions

This leads to the definition of the following research questions:

1. What are the consequences of assuming a temperature-independent ('constant') specific heat c_p per phase on the results of an enthalpic lattice Boltzmann method-based numerical simulation of heat transfer inside a material, which results in a phase transition?

2. What is the most simple, efficient and accurate lattice Boltzmann method scheme to incorporate the effect of a temperature-dependent ('variable') specific heat c_p?

3. Do the proposed LBM schemes which incorporate the effect of a temperature-dependent specific heat c_p reflect reality?

1.3.2. Thesis Outline

In this chapter, a description of the MSFR and a short introduction to the lattice Boltzmann method were given. In addition, an overview of the existing literature and the relevance of the research regarding the research questions were given. In order to answer these research questions, in chapter 2 an overview is given of the relevant theory, which exists of governing equations and insights that fundamentally underlie the heat transfer processes and the lattice Boltzmann method. In chapter 3, the principles underlying the different lattice Boltzmann method schemes are discussed, and the three evaluated cases are defined. In chapter 4, a clarification is given for the experimental procedure used to test the third research question by measuring the propagation of a paraffin melting front. In chapter 5, the results of the numerical simulations and experimental measurements for the various cases are shown and discussed. The thesis is concluded and recommandations for further research are given in chapter 6.

2

Theory

In order to understand the heat transfer processes and the model used to simulate these heat transfers, it is necessary to understand the underlying theories that form the foundation of these processes. First, in chapter 2.1, the field of thermodynamics will be discussed, followed by section 2.2 which will discuss the underlying theory of the method used to simulate the heat transfer: the lattice Boltzmann method.

2.1. Thermodynamics

2.1.1. Main Equations

Phase changes play a big role in the thermodynamics of certain systems when assessing the heat diffusion. In these phase-change situations, using the temperature solely as a parameter does not give a complete picture, since this parameter does not account for the energy which is used or released by the latent heat. The total enthalpy is a more useful tool for assessing these phase-change situations. For the numerical implementation of the total enthalpy, it is convenient to split the total enthalpy in two components; the sensible heat, which is the energy related to the temperature change of a material without any phase changes, and the latent heat, which is released or used during a phase change.

$$H^\phi = f_l^\phi L + h^\phi = f_l^\phi L + \int_{T_{\text{ref}}}^{T} c_p dT \tag{2.1}$$

where H denotes the total enthalpy and ϕ denotes the phase of the material, with 's' for solid, 'l' for liquid, and 'm' for mushy (the phase while in transition between solid and liquid). Furthermore, L denotes the latent heat and f_l^ϕ denotes the liquid fraction of the material:

$$f_l = \begin{cases} 0 & \text{if } H < H_s \text{ (solid)} \\ \frac{H - H_s}{H_l - H_s} & \text{if } H_s \leq H \leq H_l \text{ (mushy)} \\ 1 & \text{if } H > H_l \text{ (liquid)} \end{cases} \tag{2.2}$$

where H_s denotes the highest enthalpy in which the system is still in a solid phase and H_l denotes the lowest enthalpy in which the system is still in a liquid phase. The equation for the enthalpy balance of a system reads [26]

$$\rho^\phi \frac{D}{Dt} H^\phi = q''' - \nabla \cdot \vec{q}'' + \frac{Dp}{Dt} + \overline{\overline{\tau}} : \nabla \vec{u} \tag{2.3}$$

with ρ^ϕ the density, q''' the internal heat production, $\vec{q}''$ the heat flux, p the pressure, $\overline{\overline{\tau}}$ the viscous stress tensor, $\vec{u}$ the fluid velocity and the material derivative $\frac{D}{Dt} H^\phi = \frac{\partial}{\partial t} H^\phi + \vec{u} \cdot \nabla h^\phi$. Assuming there

is no internal heat production ($q''' = 0$), no viscous dissipation ($\overline{\overline{\tau}} : \nabla \vec{v} = 0$) and in the absence of shock waves ($\frac{Dp}{Dt} = 0$), this equation can be simplified to [26]

$$\rho^{\phi} \frac{D}{Dt} H^{\phi} = -\nabla \cdot \vec{q}'' \tag{2.4}$$

On this equation, Fourier's law for heat conduction can be applied [20, 26]

$$\vec{q}'' = -\lambda^{\phi} \nabla T^{\phi} \tag{2.5}$$

By applying Fourier's law and rewriting, the following equation is obtained:

$$\frac{D}{Dt} H^{\phi} = \frac{1}{\rho^{\phi}} \nabla \cdot (\lambda^{\phi} \nabla T^{\phi}) \tag{2.6}$$

If the latent heat can be ignored, due to no phase changes occurring, an equation with temperature on both sides of the equation can be obtained by stating that in this case, $H^{\phi} = h^{\phi}$. Rewriting gives

$$\frac{D}{Dt} T^{\phi} = \frac{1}{c_p^{\phi} \rho^{\phi}} \nabla \cdot (\lambda^{\phi} \nabla T^{\phi}) = \nabla \cdot (a^{\phi} \nabla T^{\phi}) + (\frac{\nabla \rho^{\phi}}{\rho^{\phi}} + \frac{\nabla c_p^{\phi}}{c_p^{\phi}}) \cdot (a^{\phi} \nabla T^{\phi}) \approx \nabla \cdot (a^{\phi} \nabla T^{\phi}) \tag{2.7}$$

where it is assumed that the density ρ and specific heat c_p are constant ($\nabla \rho^{\phi}, \nabla c_p^{\phi} \approx 0$). Furthermore, $a^{\phi} = \frac{\lambda^{\phi}}{\rho^{\phi} c_p^{\phi}}$ denotes the thermal diffusivity. This results in a final equation

$$\frac{D}{Dt} T^{\phi} = \nabla \cdot (a^{\phi} \nabla T^{\phi}) \tag{2.8}$$

which becomes the Heat Equation for no convection ($\vec{u} = 0$) and a constant λ^{ϕ} [20, 30]

$$\frac{\partial}{\partial t} T^{\phi} = a^{\phi} \nabla^2 T^{\phi} \tag{2.9}$$

This cannot be done in a situation where latent heat cannot be ignored, so in the case of a phase change. In this case, it is more convenient to obtain an equation with enthalpy on both sides of the equation. To achieve this, the right side of 2.6 is rewritten to

$$\frac{1}{\rho^{\phi}} \nabla \cdot (\lambda^{\phi} \nabla T^{\phi}) = \frac{1}{\rho^{\phi}} \nabla \cdot (\frac{\lambda^{\phi}}{c_p^{\phi}} (c_p^{\phi} \nabla T^{\phi})) = \nabla \cdot (a^{\phi} (\nabla h^{\phi})) + \frac{\nabla \rho^{\phi}}{\rho^{\phi}} \cdot (a^{\phi} (\nabla h^{\phi})) \approx \nabla \cdot (a^{\phi} \nabla h^{\phi}) \tag{2.10}$$

where it is assumed that the density is constant ($\nabla \rho^{\phi} \approx 0$). Since

$$\nabla h^{\phi} = c_p^{\phi} \nabla T = \nabla(c_p^{\phi} T^{\phi}) - T^{\phi} \nabla c_p^{\phi} \tag{2.11}$$

it can be stated that

$$\nabla \cdot (a^{\phi} (\nabla h^{\phi})) = \nabla \cdot (a^{\phi} (\nabla(c_p^{\phi} T^{\phi}) - T^{\phi} \nabla c_p^{\phi})) \tag{2.12}$$

This results in a final equation

$$\frac{D}{Dt} H^{\phi} = \nabla \cdot (a^{\phi} \nabla h^{\phi}) \tag{2.13}$$

$$= \nabla \cdot (a^{\phi} (\nabla(c_p^{\phi} T^{\phi}) - T^{\phi} \nabla c_p^{\phi})) \tag{2.14}$$

In a case with a constant c_p^ϕ, equation 2.13 can be simplified to

$$\frac{D}{Dt}H^\phi = \nabla \cdot (a^\phi \nabla h^\phi) = \nabla \cdot (a^\phi(\nabla c_p^\phi T^\phi)) \tag{2.15}$$

It is important to note that in order to use the right side of equation 2.13, $c_p^\phi T$ can *not* be estimated by stating $c_p^\phi T \approx h^\phi$ [1], since this would imply

$$\nabla \cdot (a^\phi \nabla h^\phi) = \nabla \cdot (a^\phi(\nabla(c_p^\phi T) - T^\phi \nabla c_p^\phi)) \approx \nabla \cdot (a^\phi(c_p^\phi \nabla T^\phi - T^\phi \nabla c_p^\phi)) = \nabla \cdot (a^\phi(\nabla h^\phi - T^\phi \nabla c_p^\phi)) \tag{2.16}$$

It becomes clear that in this approximation it is approximated that

$$\nabla h^\phi \approx \nabla h^\phi - T^\phi \nabla c_p^\phi \tag{2.17}$$

in which $-T^\phi \nabla c_p^\phi$ is the approximation error.

If this, rather large, approximation error is *still* made, the right side of equation 2.13 can be simplified by stating

$$\nabla h^\phi - T^\phi \nabla c_p^\phi = \beta_{\text{eff}} \nabla h^\phi \tag{2.18}$$

with

$$\beta_{\text{eff}} = \frac{\nabla h^\phi - T^\phi \nabla c_p^\phi}{\nabla h^\phi} = 1 - \frac{\nabla c_p^\phi}{\nabla h^\phi} T^\phi = 1 - \frac{\frac{\partial c_p^\phi}{\partial T} \nabla T}{\frac{\partial h^\phi}{\partial T} \nabla T} T^\phi = 1 - \frac{\frac{\partial c_p^\phi}{\partial T}}{c_p^\phi} T^\phi \tag{2.19}$$

This results in

$$\frac{D}{Dt}H^\phi = \nabla \cdot (\beta_{\text{eff}} \, a^\phi \nabla h^\phi) = \nabla \cdot (a_{\text{eff}}^\phi \nabla h^\phi) \tag{2.20}$$

with a_{eff}^ϕ the effective thermal diffusivity.

2.1.2. Effect of Estimating a Constant Specific Heat

By estimating a temperature-independent specific heat, an approximation is made which has an effect on the outcome of equation 2.13. Since ∇h^ϕ obtains different values for a temperature-dependent and (estimated) temperature-independent values, this has an effect on the rate of change of the total enthalpy. The value of the total enthalpy for a certain temperature is also influenced by the choice of a certain specific heat.

If equation 2.13 is developed for a temperature-independent specific heat $c_{p,c}^\phi$, one obtains

$$\frac{DH^\phi}{Dt} = \nabla \cdot (a_c^\phi \nabla h_c^\phi) = \nabla a_c^\phi \cdot \nabla h_c^\phi + a_c^\phi \nabla^2 h_c^\phi = a_c^\phi \nabla^2 (c_{p,c}^\phi T) = \frac{\lambda^\phi}{\rho} \nabla^2 T \tag{2.21}$$

with a_c^ϕ and h_c^ϕ the thermal diffusivity and specific enthalpy based on the temperature-independent specific heat $c_{p,c}^\phi$.

If equation 2.13 is developed for a temperature-dependent specific heat $c_{p,v}^\phi$, one obtains

$$\frac{DH^\phi}{Dt} = \nabla \cdot (a_v^\phi \nabla h_v^\phi) = \nabla a_v^\phi \cdot \nabla h_v^\phi + a_v^\phi \nabla^2 h_v^\phi \tag{2.22}$$

$$= a_v^\phi T \nabla(\frac{dc_{p,v}^\phi}{dT}) \cdot \nabla T + a_v^\phi(\frac{dc_{p,v}^\phi}{dT} - \frac{T}{c_{p,v}^\phi}(\frac{dc_{p,v}^\phi}{dT})^2)|\nabla T|^2 + a_v^\phi(T\frac{dc_{p,v}^\phi}{dT} + c_{p,v}^\phi)\nabla^2 T \tag{2.23}$$

---

[1]In two of the models shown in this thesis, this estimation was made. In order to understand the mathematical basis on which these models are built, the elaboration of this approximation is shown.

with a_v^ϕ and h_v^ϕ the thermal diffusivity and specific enthalpy based on the temperature-dependent specific heat $c_{p,v}^\phi$. The full derivation can be found in appendix D. The difference between equation 2.21 and 2.22 gives an insight in the approximation made by assuming an temperature-independent specific heat when this is not the case.

2.1.3. Analytical solutions

In some specific scenarios, an analytical solution can be found. This can, for instance, be done for equation 2.15. For the valid regime of this equation, a conduction-based heat transfer (no convection) with a constant λ^ϕ, ρ^ϕ and c_p^ϕ, this equation can be solved analytically for both a scenario with and without a phase change in the semi-infinite regime.

Phase change

The first scenario, in which a phase change occurs and in which the location of the boundary between the liquid and solid fraction is dependent of time, is also known as the Stefan-problem. For a one-dimensional Stefan-problem, in the domain x[0,→), an analytical solution exists if the bulk has an uniform temperature T_0 at $t = 0$. In this case, a temperature T_w is imposed on the wall at $x = 0$, resulting in a heat transfer and a mobile melting / freezing front, depending on the wall temperature and the bulk temperature. The location of the melting / freezing front $X(t)$ can be determined by [16]

$$X(t) = 2k\sqrt{a^\phi t} \tag{2.24}$$

with t the time, a^ϕ denoting a^s/a^l for a freezing / melting front and k a dimensionless parameter. This k is dependent of if there is a freezing front ($T_w < T_f$, $T_0 > T_f$) or a melting front ($T_w > T_f$, $T_0 < T_f$).

Freezing front

For a freezing front, k can be obtained by solving [16]

$$\frac{e^{-k^2}}{\text{erf}(k)} + \frac{\lambda^l}{\lambda^s}\left(\frac{a^s}{a^l}\right)^{1/2}\frac{T_f - T_0}{T_m - T_w}\frac{e^{-k^2(a^s/a^l)}}{\text{erfc}\left(k\sqrt{a^s/a^l}\right)} = \frac{kL\sqrt{\pi}}{c_p^s(T_f - T_w)} \tag{2.25}$$

with T_f / T_m the freezing / melting temperature, and erf and erfc the error function and the compatible error function respectively. The analytical solution for the temperature profile is then the following [16]:

$$T(x,t) = \begin{cases} T_w + \dfrac{(T_f-T_w)\,\text{erf}(\frac{x}{2\sqrt{a^s t}})}{\text{erf}(k)} & \text{if } 0 < x < X, t > 0 \text{ (solid)} \\[3mm] T_0 + \dfrac{(T_f-T_0)\,\text{erfc}(\frac{x}{2\sqrt{a^l t}})}{\text{erfc}(k\sqrt{\frac{a^s}{a^l}})} & \text{if } x \geq X(t), t > 0 \text{ (liquid)} \end{cases} \tag{2.26}$$

Melting front

For a melting front, k can be obtained by solving [16]

$$\frac{e^{-k^2}}{\text{erf}(k)} + \frac{\lambda^s}{\lambda^l}\left(\frac{a^l}{a^s}\right)^{1/2}\frac{T_f - T_0}{T_m - T_w}\frac{e^{-k^2(a^l/a^s)}}{\text{erfc}\left(k\sqrt{a^l/a^s}\right)} = \frac{kL\sqrt{\pi}}{c_p^l(T_w - T_f)} \tag{2.27}$$

with T_f / T_m the freezing / melting temperature, and erf and erfc the error function and the compatible error function respectively. The analytical solution for the temperature profile is then the following [16]:

$$T(x,t) = \begin{cases} T_w + \dfrac{(T_f-T_w)\,\text{erf}(\frac{x}{2\sqrt{a^l t}})}{\text{erf}(k)} & \text{if } 0 < x < X, t > 0 \text{ (liquid)} \\[3mm] T_0 + \dfrac{(T_f-T_0)\,\text{erfc}(\frac{x}{2\sqrt{a^s t}})}{\text{erfc}(k\sqrt{\frac{a^l}{a^s}})} & \text{if } x \geq X(t), t > 0 \text{ (solid)} \end{cases} \tag{2.28}$$

No phase change

The second scenario, with no phase change occurring during heat transfer, is also known as the penetration theorem [10]. In a one-dimensional situation, in the domain x[0,→), an analytical solution exists if the bulk has an uniform temperature T_0 at $t = 0$. In this case, a temperature T_w is imposed on the wall at $x = 0$, resulting in a heat transfer. The temperature profile is then the following [10]:

$$T(x,t) = T_0 + (T_w - T_0) \operatorname{erfc}(\frac{x}{2\sqrt{a^\phi t}}) \tag{2.29}$$

with a^ϕ denoting a^s / a^l for the heat transfer problem to occur in a solid / liquid material.

2.2. Boltzmann equation

In order to understand the lattice Boltzmann method (LBM) used to simulate heat transfer, the Boltzmann equations should be discussed first. The LBM is based on the Boltzmann equations. The most standard LBM, which simulates fluid dynamics, is a second-order accurate solver for the weakly compressible Navier-Stokes equation [5, 20].

$$\rho \frac{D\vec{u}}{Dt} = -\nabla p + \rho \nabla \cdot (\nu \nabla \vec{u}) + \vec{F} \tag{2.30}$$

with the viscosity ν and the body force $\vec{F}$. The similarities with the enthalpy balance in equation 2.13 become clear with the modifications [5, 20]

$$\rho \vec{u} \rightarrow \rho H, \ \rho \vec{u} \cdot \nabla \vec{u} + \nabla p \rightarrow \rho \vec{u} \cdot \nabla h, \ \nu \rightarrow a, \ \vec{F} \rightarrow q \tag{2.31}$$

with $q = 0$ in eq. 2.6 due to no present heat sources or sinks. The similarity to equation 2.8 can be found in a similar way.

The Boltzmann equation is built upon the Kinetic Theory, in which it describes particles on a mesoscopic scale. This means that instead of following the motion of individual particles (microscopic) or only macroscopic properties like temperature and pressure, the particle distribution is followed. Therefore, the particle distribution function $f(\vec{x}, \vec{\xi}, t)$ is introduced, which represents the density of particles with location x and particle velocity ξ at time t [20]. The macroscopic variables mass density and momentum density can be found by integrating over the particle distribution function [20]:

$$\rho(\vec{x},t) = \int f(\vec{x},\vec{\xi},t)d^3\xi \tag{2.32}$$

$$\rho(\vec{x},t)\vec{u}(\vec{x},t) = \int \vec{\xi}f(\vec{x},\vec{\xi},t)d^3\xi \tag{2.33}$$

The rate of change of this particle distribution function is [20]

$$\frac{df(\vec{x},\vec{\xi},t)}{dt} = \frac{\partial f(\vec{x},\vec{\xi},t)}{\partial t} + \vec{\xi} \cdot \frac{\partial f(\vec{x},\vec{\xi},t)}{\partial \vec{x}} + \frac{\vec{F}}{\rho} \cdot \frac{\partial f(\vec{x},\vec{\xi},t)}{\partial \vec{\xi}} \equiv \Omega(f) \tag{2.34}$$

In which the first two terms of the middle equation represent the particle velocities and the term on the right represents the change in these particle velocities, hence the force $\vec{F}$ which causes these velocity changes is involved in this term [5, 20]. $\Omega(f)$ is called the collision operator, due to the fact that the particle distribution function $f(\vec{x}, \vec{\xi}, t)$ is redistributed due to collisions of particles, which redistribution is captured by the collision operator [20].

It is assumed that, if one leaves a certain particle distribution alone for a certain time, the particle distribution f approaches an equilibrium distribution f^{eq}. One can then use the BGK model to state that a non-equilibrium particle distribution f will relax back to an equilibrium state f^{eq} in a certain characteristic relaxation time τ via the BGK collision operator [20]

$$\Omega(f) = -\frac{1}{\tau}(f - f^{\text{eq}}) \tag{2.35}$$

named after its inventors Bhatnagar, Gross and Krook. This relaxation time τ has a great influence on the speed at which a non-equilibrium particle distribution f relaxes back to an equilibrium state f^{eq} and its value is therefore coupled to the thermal diffusivity a^{ϕ} [20]. This will be further discussed in chapter 3.2. Via a method called the Chapman-Enskog analysis, it can be shown that the Navier Stokes equations can be derived from the Boltzmann equation [20]. These solutions can be numerically found using the lattice Boltzmann method, which will be elaborated in chapter 3. Due to the large similarity between the Navier Stokes equations and the enthalpy balance equation, the enthalpy balance equation can be numerically solved as well by using an adapted version of the standard lattice Boltzmann method.

<p style="text-align: right; font-size: 4em;">3</p>

Numerical Method

The numerical method used for this thesis is, as stated above, the lattice Boltzmann method (LBM), which is based on the equations which can be found in chapter 2.2. The LBM will be used to find solutions for the governing equations which can be found in chapter 2.1.1. In chapter 3.1, the most common variant of the LBM is introduced, used to solve fluid dynamics. In chapter 3.2, this LBM is slightly altered for it to be used for the heat transfer problems of this thesis. In chapter 3.3, two variants of the enthalpic lattice Boltzmann method (HLBM) that can account for the extra term $-T\nabla c_p$ in the enthalpy balance equation are worked out. In chapter 3.4 and 3.5 remaining steps to build the HLBM for this thesis are discussed. In chapter 3.6 an overview of the algorithm of the model is given. In chapter 3.7 and 3.8, it is discussed how the earlier discussed HLBM models are implemented in three cases in order to answer the research questions.

3.1. Lattice Boltzmann Method (LBM)

To numerically solve the Boltzmann equation, the particle distribution functions are discretized by discretizing the particle velocity. This leads to the discrete-velocity distribution function $f_i(\vec{x}, t)$ at location $\vec{x}$ and time t, with the subscript i denoting the particle velocity via $\vec{c}_i = (c_{ix}, c_{iy}, c_{iz})$ [20]. The mass density ρ and momentum density $\rho\vec{u}$ at $(\vec{x}, t)$ can be found via (weighted) sums of all $f_i(\vec{x}, t)$ [20]:

$$\rho(\vec{x}, t) = \sum_i f_i(\vec{x}, t) \tag{3.1}$$

$$\rho\vec{u}(\vec{x}, t) = \sum_i \vec{c}_i f_i(\vec{x}, t) \tag{3.2}$$

Not only the particle velocities are discretized. To give the LBM a finite resolution, the location $\vec{x}$ is discretized in a square or cubical lattice, with lattice spacing Δx. Furthermore, the time is discretized in time steps with Δt [20].

Analogously to equation 2.34, with the discrete-velocity distribution function the lattice Boltzmann equation can be formed [20]:

$$f_i(\vec{x} + \vec{c}_i\Delta t, t + \Delta t) = f_i(\vec{x}, t) + \Omega_i(\vec{x}, t) \tag{3.3}$$

with the discretized BGK collision operator [20]

$$\Omega_i(\vec{x}, t) = -\frac{f_i - f_i^{eq}}{\tau}\Delta t \tag{3.4}$$

Equation 3.3 represents the collisions and streaming of f_i to a location $\vec{x} + \Delta\vec{x} = \vec{x} + \vec{c}_i\Delta t$ at the next time step $t + \Delta t$. For numerical convenience, it is important that all f_i stream exactly to another defined

location in the square or cubical lattice during the time step Δt. To achieve this in a convenient way, it is often chosen to work in lattice units in the LBM. This implies that in lattice units, $\Delta x = 1\ \ell s$ and $\Delta t = 1\ \ell t$ [20]. To work in lattice units, all SI-units need to be converted into lattice units. More about this can be found in chapter 3.5. Furthermore, $\vec{c}_i$ is chosen such that its components c_{ix}, c_{iy} and c_{iz} obtain either the value -1, 0 or 1 $\ell s/\ell t$. In this way, each f_i streams exactly to a neighboring lattice cell in the time step Δt. Not in each LBM-based simulation, all possible velocities $\vec{c}_i$ are used. Often, certain characteristic combinations of velocities are used, denoted by DdQq. Here, d denotes the dimension of the simulation and q denotes the number of different velocities $\vec{c}_i$ used. The most common characteristic sets used are D1Q3, D2Q9, D3Q15, D3Q19 and D3Q27 [20].

In the D1Q3 set used in this thesis, the following velocities are used.

$$\vec{c}_i = c_{ix} = \begin{cases} 0 & \text{for } i = 0 \\ 1 & \text{for } i = 1 \\ -1 & \text{for } i = 2 \end{cases} \tag{3.5}$$

The magnitude of f_i also depends on its given weight coefficient w_i. The weight coefficient w_i for the most common characteristic velocity sets scales with $|\vec{c}_i|$, with the largest weight coefficient for $|\vec{c}_i| = \vec{0}$ and a decreasing magnitude of w_i for larger $|\vec{c}_i|$. For instance, the D1Q3 set has $w_0 = \frac{2}{3}$, $w_1 = w_2 = \frac{1}{6}$. The velocities and corresponding weights form velocity sets $\{\vec{c}_i, w_i\}$ [20].

In the D1Q3 set, the weight factors are [20]

$$w_i = \begin{cases} \frac{2}{3} & \text{for } i = 0 \\ \frac{1}{6} & \text{for } i = 1, 2 \end{cases} \tag{3.6}$$

3.2. Enthalpic Lattice Boltzmann Method (HLBM)

Due to the similarities between the Navier Stokes equation and the thermal / enthalpic balance equation (resp. eq. 2.8 and 2.13, earlier discussed in chapter 2.2), heat transfer problems can be solved as well by using an adapted version of the fluid dynamic based version of the lattice Boltzmann method. In order to solve a heat transfer problem, often the thermal lattice Boltzmann method (TLBM) is used [5, 14]. In the TLBM, equation 2.8 is solved. However, because in this thesis some situations with a phase change are examined, the TLBM cannot be used for every situation. Therefore, the enthalpic lattice Boltzmann method (HLBM) is used here. In the most standard HLBM, equation 2.15 is solved. This is done by introducing a new distribution function for the temperature field $g_i(\vec{x}, t)$. In a similar way to equation 3.3 [20],

$$g_i(\vec{x} + \vec{c}_i \Delta t, t + \Delta t) = g_i(\vec{x}, t) + \Omega_i(\vec{x}, t) + Q_i(\vec{x}, t) \tag{3.7}$$

with the discretized BGK collision operator [20]

$$\Omega_i(\vec{x}, t) = -\frac{g_i(\vec{x}, t) - g_i^{\text{eq}}(\vec{x}, t)}{\tau_g(\vec{x}, t)} \Delta t \tag{3.8}$$

and Q_i being responsible for the source term q, which is set to 0 in this thesis resulting in $Q_i = 0$. In the enthalpic lattice Boltzmann method, the total enthalpy H at $(\vec{x}, t)$ can be found via the sum of all $g_i(\vec{x}, t)$ [14, 20]:

$$H(\vec{x}, t) = \sum_i g_i(\vec{x}, t) \tag{3.9}$$

To let the solutions of equation 3.7 correspond to those of the physical equation 2.15, the equilibrium distribution should be set to [14]

$$g_i^{\text{eq}} = \begin{cases} f_l^\phi L + w_i h^\phi (1 - \frac{|\vec{u}|^2}{2c_s^2}) & \text{for } i = 0 \\ w_i h^\phi (1 + \frac{\vec{c}_i \cdot \vec{u}}{c_s^2} + \frac{(\vec{c}_i \cdot \vec{u})^2}{2c_s^4} - \frac{|\vec{u}|^2}{2c_s^2}) & \text{for } i \neq 0 \end{cases} \tag{3.10}$$

with c_s the speed of sound, determined by the chosen lattice. $c_s = \sqrt{\frac{1}{3}}$ for the most standard LBM sets, including the DdQq sets mentioned in chapter 3.1 [20]. The relaxation time τ_g is logically coupled to the thermal diffusivity a^ϕ via [14]

$$\tau_g(\vec{x}, t) = \frac{1}{2} + \frac{a^\phi(\vec{x}, t)}{c_s^2 \Delta t} \tag{3.11}$$

since this is the term in eq. 2.13 which determines the speed in which the system relaxes back to an equilibrium state.

Finding the Temperature
In the case where the specific heat is temperature-independent ($c_p \neq c_p(T)$), the temperature can be calculated by the total enthalpy

$$T = \begin{cases} \frac{H}{c_p^s} & \text{if } H < H_s \text{ (solid)} \\ T_s + \frac{H - H_s}{H_l - H_s} & \text{if } H_s \leq H \leq H_l \text{ (mushy)} \\ T_l + \frac{(H - H_l)}{c_p^l} & \text{if } H > H_l \text{ (liquid)} \end{cases} \tag{3.12}$$

with T_s the temperature under which the material is solid and T_l the temperature above which the material is liquid. In the case of a temperature-dependent specific heat $c_p(T)$, the temperature needs to be solved numerically from equation 2.1.

Streaming and Collision
The lattice Boltzmann method is run mainly by performing two operations during a time step Δt: the *collision* and the *streaming* step [20]. The lattice BGK equation (LBGK) equation is obtained by filling in equation 3.7 with 3.8

$$g_i(\vec{x} + \vec{c}_i \Delta t, t + \Delta t) = g_i(\vec{x}, t) - \frac{\Delta t}{\tau_g(\vec{x}, t)}(g_i(\vec{x}, t) - g_i^{\text{eq}}(\vec{x}, t)) \tag{3.13}$$

The first step is the collision [20]:

$$g_i^*(\vec{x}, t) = g_i(\vec{x}, t) - \frac{\Delta t}{\tau_g(\vec{x}, t)}(g_i(\vec{x}, t) - g_i^{\text{eq}}(\vec{x}, t)) \tag{3.14}$$

with $g_i(\vec{x}, t)$ the distribution function before and $g_i^*(\vec{x}, t)$ after the collision step, where equation 3.10 is used to calculate g_i^{eq}. The following step is the streaming [20]:

$$g_i(\vec{x} + \vec{c}_i \Delta t, t + \Delta t) = g_i^*(\vec{x}, t) \tag{3.15}$$

in which each g_i streams to the (neighboring) cell in the time step Δt corresponding to their $\vec{c}_i$. These two steps are repeated until t reaches t_{final}. This process is schematically shown in figure 3.1. The initialization is performed by stating $g_i(\vec{x}, t = 0) = g_i^{\text{eq}}(\vec{x}, t = 0)$ [20].

3.3. Enthalpic LBM Including the Extra Term $-T\nabla c_p$

The term $-T\nabla c_p$ can not automatically be implemented in the lattice Boltzmann method when making the (erroneous) assumption made in equation 2.16. In order to do this, an adjustment to the enthalpic lattice Boltzmann equation needs to be made. In order to achieve this, two different methods are used. First, the method used in Varyazmar and Bazargan (2012) [29] is applied to the problem of this thesis. Secondly, a method in which the effective thermal diffusivity a_{eff} alters the relaxation time is used; a method which, to the authors' knowledge, was not used before.

3.3.1. Method of Varyazmar and Bazargan (2012)
In the article of Varyazmar and Bazargan (2012) [29], a modified lattice Boltzmann method is used to solve heat transfer problems with a variable thermal conductivity λ. The authors incorporated this variable thermal conductivity in equation 2.8 by adding a term D to the thermal diffusivity a:

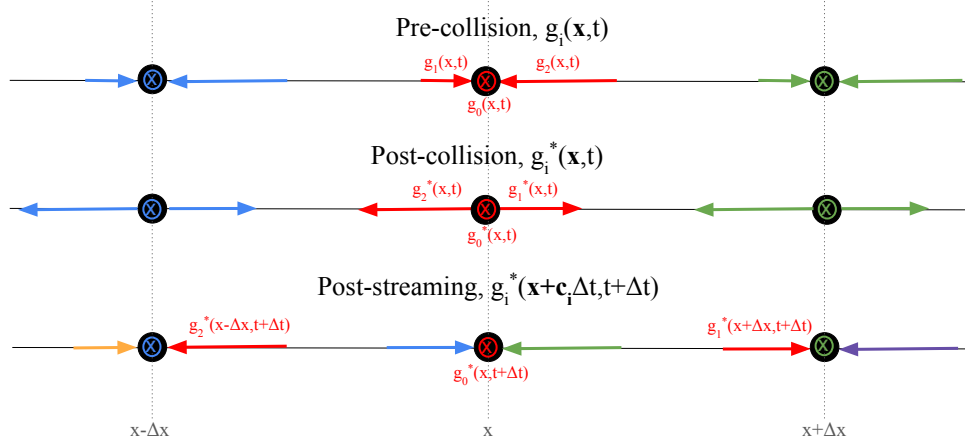$$\frac{D}{Dt}T = \nabla \cdot [(a_0 + D)\nabla T] \tag{3.16}$$

Figure 3.1: Schematic overview of the colliding and steaming process in the D1Q3 LBM scheme used in this thesis

To solve equation 3.16 with the thermic lattice Boltzmann method, the equilibrium function is adjusted to

$$g_i^{\text{eq}}(\vec{x}, t) = w_i(T + \frac{1}{c_s^2}\rho\vec{c}_i \cdot \vec{u} - \frac{D}{c_s^2}\vec{c}_i \cdot \nabla T) \tag{3.17}$$

In this thesis, not the thermal conductivity is variable, but the specific heat. But since this only has an influence on the value of the thermal diffusivity a, the same method of adding a term D to the thermal diffusivity can be expanded to the enthalpic lattice Boltzmann method for equation 2.16 used in this thesis. This results in

$$\frac{D}{Dt}H^\phi = \nabla \cdot [(a_0 + D)^\phi \nabla h^\phi] \tag{3.18}$$

The equilibrium distribution needs to be adjusted as well in reference to Varyazmar and Bazargan (2012) to fit equation 3.18

$$g_i^{\text{eq}} = \begin{cases} f_l^\phi L + w_i h^\phi & \text{for } i = 0 \\ w_i(h^\phi + \frac{1}{c_s^2}\rho\vec{c}_i \cdot \vec{u} - \frac{D}{c_s^2}\vec{c}_i \cdot \nabla h^\phi) & \text{for } i \neq 0 \end{cases} \tag{3.19}$$

To make equation 3.18 equal to equation 2.16, the term D in 3.18 should contain the additional $-T\nabla c_p$ term in 2.16.

$$\nabla \cdot [(a_0 + D)^\phi \nabla h^\phi] = \nabla \cdot (a_0^\phi \nabla h^\phi) + \nabla \cdot (D^\phi \nabla h^\phi) = \nabla \cdot (a^\phi \nabla h^\phi) - \nabla \cdot [a^\phi(T^\phi \nabla c_p^\phi)] \tag{3.20}$$

in which the leftmost two terms originate from equation 3.18 and the right term originates from equation 2.16. This shows that, for the equation to be valid

$$a^\phi = a_0^\phi, \quad D^\phi = -\frac{a^\phi T^\phi \nabla c_p^\phi}{\nabla h^\phi} \tag{3.21}$$

Substituting this in the equilibrium distribution of 3.19, we obtain the equilibrium distribution to be used to integrate this method in the situations of this thesis.

$$g_i^{\text{eq}} = \begin{cases} f_l^\phi L + w_i h^\phi & \text{for } i = 0 \\ w_i(h^\phi + \frac{1}{c_s^2}\rho\vec{c}_i \cdot \vec{u} + \frac{a^\phi T^\phi \nabla c_p^\phi}{c_s^2} \cdot \vec{c}_i) & \text{for } i \neq 0 \end{cases} \tag{3.22}$$

In order to use this equilibrium function, ∇c_p has to be calculated. This is not ideal, since this cannot be done locally with just the data of the cell for which g_i^{eq} is calculated itself; the data of the surrounding

cells are required as well. An additional problem is that a possible mobile melting / freezing front requires additional conditions that specify which surrounding cells can be used to calculate ∇c_p with. The algorithm in which ∇c_p is calculated depends on the choice of the algorithm to be first- or second-order accurate. The algorithm of both can be found in the appendix A.

The choice between both seems obvious, but a second-order accurate system has some disadvantages. The main disadvantage is that, unless at least three cells in a row in a certain direction have the same phase, ∇c_p must be set to 0 in that direction. Otherwise, there are not enough cells with the same phase to calculate ∇c_p via equation A.2, A.4 and A.5. For situations with a large ∇c_p and a relatively small number of cells in a certain direction in the numerical model, this can lead to large errors in the first few time steps. If the first- or second-order accurate algorithm should be used to calculate ∇c_p should therefore be carefully considered by the user of the model.

3.3.2. Effective Thermal Diffusivity method

The Effective Thermal Diffusivity method is based on equation 2.20. This equation is very similar to equation 2.13, with the only difference that a^{ϕ} in 2.15 becomes $a^{\phi}_{\text{eff}} = \beta^{\phi}_{\text{eff}} a^{\phi}$ in 2.20. Therefore, the normal Enthalpic Lattice Boltzmann method of chapter 3.2 can be used, with the only difference in the calculation of the relaxation time τ_g (see eq. 3.11), which becomes

$$\tau_g = \frac{1}{2} + \frac{a^{\phi}_{\text{eff}}}{c_s^2 \Delta t} = \frac{1}{2} + \frac{\left(1 - \frac{\partial c_p^{\phi}/\partial T}{c_p^{\phi}} T^{\phi}\right) a^{\phi}}{c_s^2 \Delta t} = \frac{1}{2} + \frac{a^{\phi}}{c_s^2 \Delta t} - \frac{(\partial c_p^{\phi}/\partial T) \, T^{\phi}}{c_p^{\phi}} \frac{a^{\phi}}{c_s^2 \Delta t} \tag{3.23}$$

Since this method is local (no data of surrounding cells is needed) and independent of the direction of the heat flow and mobile phase fronts in multidimensional models, this is a far easier to implement method to solve equation 2.13 than the Varyazmar and Bazargan (2012) [29] based method described in chapter 3.3.1. Furthermore, this model has a smaller error than the Varyazmar and Bazargan (2012) based method since there is no necessity to have at least two or three connecting cells with the same phase in order for the model to work properly. An important note is that in the mushy zone of a chemically pure substance, $\frac{\partial c_p^m}{\partial T}$ is set to 0, since in the case of such a substance the mushy zone exists of only one (phase-change) temperature. This implies that $\frac{\partial c_p^m}{\partial T}$ is not defined.

3.4. Boundary conditions

Since the lattice Boltzmann method is a numerical method, it is very important to have well-suited boundary conditions for the model. The interactions of the particles in the bulk of the model itself are, namely, of a similar importance as the interactions between the bulk and the boundaries of the model. In the LBM-based model used for this thesis, link-wise boundaries are used. Here, the boundaries lie on the lattice links, so in between two lattice cells [20]. The boundary conditions implemented throughout this thesis will follow the so-called bounce-back scheme. This scheme is visually represented in figure 3.2.

The implementation of this scheme can, for instance, be found for the boundaries, which now will be called "walls", at which *no* temperature is imposed (in this thesis: the right wall). In the cells next to these walls, the distribution functions heading towards the wall leave the node at a time t and meet the wall at $t + \frac{1}{2}\Delta t$. Numerically, at the wall, these distribution functions make a 180°-degree turn and flow back to the node they originally left, where they arrive at $t + \Delta t$. This process takes place solely during the streaming step. The streaming step for the distribution functions in the direction of the wall originating from the nodes at the boundaries can be summarized by

$$g_{\bar{i}}(\vec{x}, t + \Delta t) = g_i^*(\vec{x}, t) \tag{3.24}$$

with $f_{\bar{i}}$ being a distribution function for which $c_{\bar{i}} = -c_i$ [20].

For the walls where a temperature *is* imposed, an anti-bounce-back scheme is used. In this thesis, for walls where a temperature is imposed, a Dirichlet boundary condition is used. Thus, the wall has a

fixed temperature at which the distribution functions reflect back, leading to the following change in magnitude [20]:

$$g_{\bar{i}}(\vec{x}, t + \Delta t) = -g_i^*(\vec{x}, t) + 2g_i^{\text{eq}}(\vec{x}_w, t + \Delta t) \tag{3.25}$$

Here, the equilibrium term is calculated by using equation 3.10 or 3.22, in which the sensible heat h^ϕ is determined based on the wall temperature and the thermophysical properties of the material in which the heat transfer takes place next to the wall.
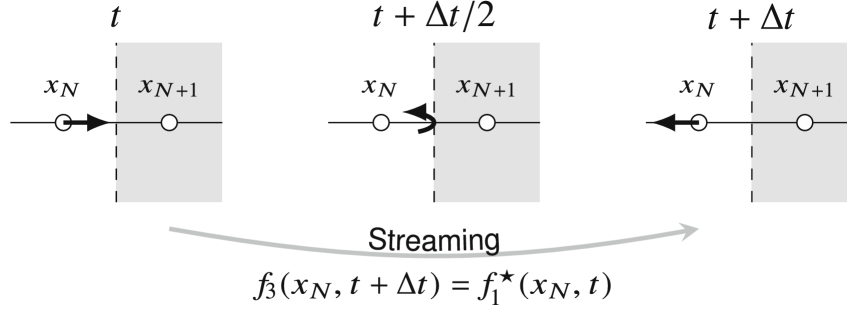

Figure 3.2: Illustration of the streaming step according to the like-wise bounce-back-scheme used in this thesis, obtained from Krüger et al. [20]

3.5. Unit Conversion and Stability Requirements

As discussed earlier in chapter 3.1, the convenient units to use in the lattice Boltzmann method are lattice units. These units are characterized by setting $\Delta x^* = 1\ \ell s$ and $\Delta t^* = 1\ \ell t$ in the lattice units. In this chapter (3.5), lattice units are denoted by an asterisk *, which is left out in the rest of the report. The physical values of the parameters used in the LBM, which are often in SI-units, can be translated to lattice units via a conversion factor C [20]

$$y^* = \frac{y}{C_y} \tag{3.26}$$

In which y can be any parameter and C_y is its conversion factor. Since $\Delta x^* = 1\ \ell s$ and $\Delta t^* = 1\ \ell t$, $C_l = \Delta x$ (l for 'length') and $C_t = \Delta t$. Furthermore, $C_\rho = \rho$ and $C_T = 1\ \ell K$ are often chosen in the LBM [20]. With this basis, all relevant parameters can be converted from SI units to lattice units, such as the conversion unit for the enthalpy C_h, thermal diffusivity C_a, specific heat C_{c_p} [6]:

$$C_h = \frac{C_l^2}{C_t^2}, \quad C_a = \frac{C_l^2}{C_t}, \quad C_{c_p} = \frac{C_l^2}{C_t^2 C_k} \tag{3.27}$$

In order to have a stable simulation, $\frac{\tau^*}{\Delta t^*} = \tau^* \geq \frac{1}{2}$ [20]. The closer τ is to 0.5, the longer it takes the simulation to converge to the solution. Since τ is coupled to the conversion factors C_l and C_t via equations 3.11 or 3.23 and 3.27, it can be found that for a τ closer to 0.5, the resolution of the simulation increases as well, resulting in a larger computational burden. The larger τ^* is, the larger the error is in the simulation, since the simulation truncation error scales with $(\tau^* - \frac{1}{2})^2$ [20]. Therefore, it is important to choose τ wisely to reduce this error as much as possible, but without making the model unnecessarily computationally expensive and not converged.

In order to achieve this, in the model used in this thesis, the user of the model does not choose Δt, but rather the desired lowest value of τ^* in the simulation. Then, with equation 3.11 or 3.23, the lowest value of a_{low}^* within the temperature domain of a certain heat transfer case is calculated. This results in the value of the conversion factor C_a.

$$C_a = \frac{a_{\text{low}}}{a_{\text{low}}^*} \tag{3.28}$$

with a_{low} the lowest value corresponding to the temperature range of the model. Then C_t can be calculated via C_l and C_a

$$C_t = \frac{C_l^2}{C_a} \tag{3.29}$$

3.6. Algorithm overview

The numerical method used is implemented in the Julia coding language, which was run in Jupyter Notebooks hosted by Anaconda Navigator. In order to get an insight in the way the simulations are run, a general version of the implemented lattice Boltzmann methods algorithm is schematically shown in figure 3.3. These steps are clarified below:

1. First, the libraries Plots.jl, LaTeXStrings.jl, Roots.jl and SpecialFunctions.jl are imported, and the model parameters which can be chosen by the models user are set: the relaxation time τ_g, wall temperature T_w, initial bulk temperature T_0, spatial resolution Δx, length of the simulation x_{end} and end time of the simulation t_{end} or t_{max}.

2. Based on these set parameters, the remaining conversion factors (see ch. 3.5) and model parameters are defined, such as the number of cells and time steps used in the model based on the spatial and temporal resolution of the model. Furthermore, the macroscopic properties are defined, such as the functions for c_p, h, f_l, a etc. over temperature or enthalpy.

3. Then, the functions to calculate the equilibrium distributions are defined. One equilibrium distribution, eq. 3.10, is sufficient for all but the LBM based on Varyazmar and Bazargan (2012) [29]. For the latter, multiple equilibrium functions based on eq. 3.22 are required, since the method of determining ∇c_p is dependent of the location of the cell, its phase and the location of the melting/freezing front. These different methods can be found in the appendix A.

4. Based on these functions that calculate the equilibrium distribution and the macroscopic property functions, the initial distributions and last initial conditions can be defined (see ch. 3.2).

5. Then, a loop starts in which the heat transfer is simulated. Each loop exists of one time step and is run until the time reaches t_{max} / t_{end}.

    a) First, the equilibrium function for each cell is calculated, based on its current value of H and T, according to eq. 3.10 or 3.22. Furthermore, the relaxation time τ_g for each cell is calculated according to eq. 3.11 or 3.23.

    b) Then, the collision step takes place, according to equation 3.14.

    c) Subsequently, the anti-bounce-back scheme (eq. 3.25) on the wall with the implied temperature and the bounce-back scheme (eq. 3.24) on the other walls are implemented, since these depend on the after-collision distribution functions.

    d) This is followed by the streaming step for all cells, in which the distribution functions flow from one cell to another corresponding to their velocity, according to eq. 3.15.

    e) Then, the new H-value for each cell can be calculated by summing the distribution functions per cell (equation 3.9).

    f) Using this new H, T and f_l can be calculated for each cell by resp. solving for T in eq. 2.1 or 3.12 and using eq. 2.2. The melting front (if applicable) propagation is determined by summing the liquid fraction of all cells and multiplying it by the spatial resolution in SI-units. The freezing front (if applicable) is determined by subtracting the sum of the liquid fraction of all cells of the total number of cells and multiplying this by the spatial resolution in SI-units

    g) Then, some of the data is saved in order to make plots over time. At least the data of f_l are saved in order to visualize the ice front over time.

6. If the simulation is run, the temperature profile and ice layer are plotted over resp. distance and time.

3.7. Method of Assessment

In order to answer the research questions, three heat transfer cases are numerically assessed. In the first and second case, a freezing front in water is simulated, with different wall temperatures between the cases. In the third case, a melting front in paraffin is assessed, both numerically and experimentally. More details about these cases can be found in chapter 3.8. This choice of cases was made in order to answer the research questions as completely as possible. To do this, in the following section the
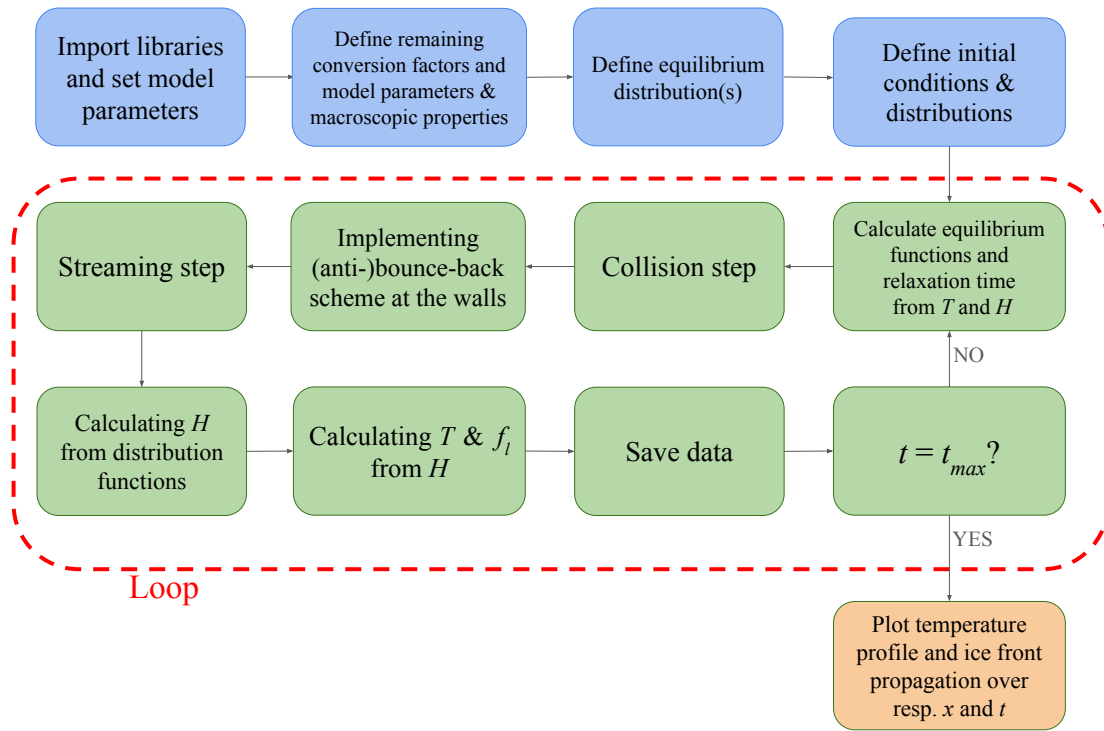
Figure 3.3: Schematic overview of the general LBM algorithm used in this thesis

focus is shifted from the details about the implementation of various lattice Boltzmann methods to the methodology how useful information can be extracted from these models.

3.7.1. Implementation of the Models

When considering all cases, six different models are implemented, which were elaborated earlier.

1. **Analytical:** The analytical model for a temperature-independent specific heat (see chapter 2.1.3)

2. **TI-HLBM:** The enthalpic LBM numerical model for a temperature-independent specific heat (see chapter 3.2)

3. **TD-HLBM** The enthalpic LBM numerical model for a temperature-dependent specific heat (see chapter 3.2)

4. **TI-HLBM-VB:** The enthalpic LBM numerical solution based on Varyazmar and Bazargan (2012) [29] for a temperature-independent specific heat (see chapter 3.3.1)

5. **TD-HLBM-VB:** The enthalpic LBM numerical model based on Varyazmar and Bazargan (2012) [29] for a temperature-dependent specific heat (see chapter 3.3.1)

6. **TD-HLBM-a_{eff}:** The enthalpic LBM numerical model based on the effective thermal diffusivity method for a temperature-dependent specific heat (see chapter 3.3.2)

In case 1 and 2, all six models are implemented. In case 3, only the results of models 1, 2 and 3 are assessed. The parameters used in these cases can be found in section 3.8

3.7.2. Evaluation of the Implemented Models

The implemented models per case are first evaluated in general, by showing and comparing their solutions to each other for the temperature profile over distance after t_{max} and the front propagation over time.

Secondly, the numerical influence of different temperature-independent estimations for the temperature-dependent specific heat is evaluated. In order to do this, various combinations of temperature-independent specific heats for the solid and liquid phase are used in the TI-HLBM model. The results

are compared to the numerical solutions of the TD-HLBM model by calculating the relative error of the TI-HLBM model to the TD-HLBM model. For the error calculation, see section 3.7.3

Temperature-Independent Estimate Pairs Used
In the assessment of the numerical influence of different temperature-independent estimations, five different solid/liquid estimation pairs are used. The basic estimate is for solid/liquid state the specific heat at resp. the freezing/melting temperature. The other four estimates are based on the freezing/melting, wall and bulk temperature; they are determined by calculating the c_p value for temperatures based on different ratios between the freezing/melting temperature and the wall temperature T_w or initial bulk temperature T_0. For these calculations, the functions for the temperature-dependent specific heat stated in Appendix B are used.

Two methods of estimate pairing for the solid/liquid specific heat are used, in order to find the pair that, when inserted in the TI-HLBM model, results in the greatest similarity between this and the TD-HLBM model.

"distance from $T_{f/m}$": In the first method, the best fitting estimate solid/liquid pair is found by calculating the specific heat from the temperature-dependent specific heat function, using temperatures with the same ratio in the amount of deviation from the melting/freezing temperature towards the extreme temperature of their phase (T_w or T_0).

"low to high": In the second method, the best fitting estimate pair is again found by calculating the specific heat from the temperature-dependent specific heat function, now using temperatures with the same ratio of the amount of deviation from the temperature extreme with the lowest specific heat of their phase towards the extreme with the highest specific heat of their phase. In this method, it is assumed that in the investigated temperature regime, the specific heat is constantly increasing or decreasing over temperature.

Validation of Reliability HLBM models
In the results section, three methods of validation are used in order to validate the reliability of the results resulting from the implemented models per case.

1: In this practice, the solution of the analytical model is used to benchmark the numerical solution for the TI-HLBM model, since these two models should present exactly the same result in the case of a perfect numerical simulation. If these models show similar results for certain parameters in the enthalpic LBM-based model, this validates the use of these parameters for this and the other enthalpic LBM-based models used to obtain reliable results. In order to show the similarity between the analytical and TI-HLBM model for various spatial resolutions and the dependence of this similarity on the spatial resolution, the relative error from the TI-HLBM model to the analytical model is shown in the results section as well. The calculation of the error can be found in section 3.7.3.

2: Furthermore, the TI-HLBM-VB model is used to validate the usage of both this model and the TD-HLBM-VB model by comparing it to the TI-HLBM model. The results of the TI-HLBM-VB and TI-HLBM model should be the same, since the first compensates the last model for the extra term $-T\nabla c_p^\phi$, which is zero for a temperature-independent specific heat. If this similarity is found, this is an indication of the validity of the TD-HLBM-VB models solutions.

3: Lastly, the TD-HLBM-VB and TD-HLBM-a_{eff} model should show similar results, since exactly the same input is given in both methods, of which it is believed that they both can compute the correct solution of the given heat problem.

3.7.3. Error Calculation
Between Analytical and TI-HLBM Model
The similarity between the analytical solution and the numerical solution for the TI-HLBM model is determined by calculating the average relative error in the melting/freezing front propagation ϵ_{fr} and in the temperature profile ϵ_T [6]:

$$\epsilon_{fr/T} = \frac{1}{N_{t/x}} \sum_i^{N_{t/x}} |\frac{\text{TI-HLBM}_{i,fr/T} - \text{Analytical}_{i,fr/T}}{\text{Analytical}_{i,fr/T}}| \tag{3.30}$$

with $N_{t/x}$ the number of time steps/lattice cells in the numerical solution. These relative errors often follow the relation

$$\epsilon_{fr} = C_{fr}(\frac{\Delta x}{x_{end}})^m, \quad \epsilon_T = C_T(\frac{\Delta x}{x_{end}})^n \tag{3.31}$$

with m the convergence coefficient of the front and n of the temperature.

Between TI-HLBM and TD-HLBM model

The relative error between the numerical solutions of the TI- and TD-HLBM model are calculated for both the temperature profile and the freezing/melting front propagation. This relative error is not given single valued, such as the error between the analytical solution and the temperature-independent specific heat, but is presented per data point, such that a pattern in the relative error over resp. distance and time can be found. The errors ϵ are calculated via

$$\epsilon_{i,fr/T} = \frac{\text{TI-HLBM}_{i,fr/Tx} - \text{TD-HLBM}_{i,fr/T}}{\text{TD-HLBM}_{i,fr/T}} \tag{3.32}$$

with $\text{HLBM}^{TI}_{i,fr/T}$ and $\text{HLBM}^{TD}_{i,fr/T}$ the numerical solution of resp. the TI- and TD-HLBM model.

3.8. Numerically Assessed Cases

In order to pose an answer to the research questions, three heat transfer cases are numerically assessed.

3.8.1. General Overview of the Cases

The assessed cases have some similarities. In all cases, the heat transfer is studied with multiple enthalpic lattice Boltzmann method schemes discussed in chapter 3.7.1. This is done in one dimension, according to the D1Q3 scheme. In the simulations, the bulk material has a uniform initial temperature T_0. At the left wall, a wall temperature T_w is imposed. The interaction between the bulk and the left / right wall is determined by resp. the anti-bounce-back / bounce-back scheme (eq. 3.25 / 3.24). The heat transfer in all cases is based on diffusion. No convection takes place, which implies $\vec{u} = \vec{0}$. Furthermore, for all cases, the lowest value of τ_g was set at 0.545.

For all cases, first, the main parameters used are shown in a tabular. Secondly, the temperature-independent estimate pairs for the temperature-dependent specific heat, used in the assessment of their influence on the numerical solution per case (see section 3.7.1), are shown.

3.8.2. Case 1 - Simulating Freezing Front in Water

Main Parameters

For this first case, a freezing front in water is evaluated. The parameter values used can be found in table 3.1.

Table 3.1: Thermophysical properties used in the numerical model for case 1 in SI- and LBM-units. The origin of the values of L, λ^ϕ and ρ_0 can be found in Appendix B.1

Variable	Description	SI-units	LBM-units
x_{end}	Simulation length	0.12 m	192 ℓs
T_f	Freezing temperature	273.15 K	273.15 ℓK
T_0	Initial temperature	276 K	276 ℓK
T_w	Left wall temperature	230 K	230 ℓK
L	Latent heat	334 kJ/kg	$1.71 \cdot 10^9$ $\ell s^2/\ell t^2$
$\lambda^{s/l}$	Thermal conductivity	2.10/0.55 W/mK	$0.300/0.0787$ $\ell s/\ell t^3\ell K$
c_p^ϕ	Specific heat	See Table 3.2	$5122 \cdot c_p^\phi$ $\ell s^2/\ell t^2\ell K$
ρ_0	Density	1000 kg/m^3	$2.441 \cdot 10^{-7}$ ℓs^{-3}

Estimate Pairs Specific Heat

The "distance from $T_{f/m}$" and "low-to-high" methods in case 1 lead to the same estimate pairs of the temperature-dependent specific heat, due to the decreasing nature of $c_p^l(T)$ in the temperature region

used in case 1 (273-276 K). Therefore, only 5 estimation pairs are evaluated, which can be found in tabular 3.2.

Table 3.2: Definition of the specific heats used in the numerical model for case 1 in SI- and LBM-units. The origin of the values can be found in Appendix B.1

Variable	SI-units (J/kgK)	LBM-units ($\ell s^2/\ell t^2 \ell K$)
$c_p^\phi(T)$	See Appendix B.1	$5122 \cdot c_p^\phi$
$c_p^{s/l}(T_f/T_f)$	2066/4217	$1.058 \cdot 10^7 / 2.160 \cdot 10^7$
$c_p^{s/l}(T_f - \frac{1}{4}(T_w - T_f)/T_f + \frac{1}{4}(T_0 - T_f))$	1992/4214	$1.020 \cdot 10^7 / 2.158 \cdot 10^7$
$c_p^{s/l}(T_f - \frac{1}{2}(T_w - T_f)/T_f + \frac{1}{2}(T_0 - T_f))$	1918/4211	$9.822 \cdot 10^6 / 2.157 \cdot 10^7$
$c_p^{s/l}(T_f - \frac{3}{4}(T_w - T_f)/T_f + \frac{3}{4}(T_0 - T_f))$	1844/4209	$9.444 \cdot 10^6 / 2.156 \cdot 10^7$
$c_p^{s/l}(T_w/T_0)$	1770/4206	$9.064 \cdot 10^6 / 2.155 \cdot 10^7$

The specific heat of the mushy zone is calculated according to Appendix B.1.

Since the estimate pairs for both hypotheses coincide for case 1 and 2, an additional research is conducted for these cases: the best-fitting pair is investigated for a lower spatial resolution, to determine if the results can be extrapolated into different resolutions.

In the lower spatial resolution simulation used, the simulation length is 96 ℓs. Since this is two times lower than the length of the simulation described in table 3.1, all values in LBM-units decrease or increase corresponding to the dimension of ℓs in the unit.

3.8.3. Case 2 - Simulating Freezing Front in Water

Main Parameters
The second case is identical to the first case, exept for a (much) lower wall temperature T_w, which is shown in tabular 3.3.

Table 3.3: Thermophysical properties used in the numerical model for case 2 which deviate from those in case 1, in SI- and LBM-units. For the remaining parameters, see tabular 3.1.

Variable	Description	SI-units	LBM-units
T_w	Left wall temperature	100 K	100 ℓK

Estimate Pairs Specific Heat
Due to the similarity between case 1 and 2, the "distance from $T_{f/m}$" and "low-to-high" methods in case 2 lead to the same estimate pairs of the temperature-dependent specific heat as well, due to the decreasing nature of $c_p^l(T)$ in the temperature region used in case 1 (273-276 K). Therefore, again only 5 estimation pairs are evaluated, which can be found in tabular 3.4.

Table 3.4: Definition of the specific heats used in the numerical model for case 2 in SI- and LBM-units. The origin of the values can be found in Appendix B.1

Variable	SI-units (J/kgK)	LBM-units ($\ell s^2/\ell t^2 \ell K$)
$c_p^\phi(T)$	See Appendix B.1	$5122 \cdot c_p^\phi$
$c_p^{s/l}(T_f/T_f)$	2066/4217	$4.742 \cdot 10^7 / 9.680 \cdot 10^7$
$c_p^{s/l}(T_f - \frac{1}{4}(T_w - T_f)/T_f + \frac{1}{4}(T_0 - T_f))$	1768/4214	$4.058 \cdot 10^7 / 9.673 \cdot 10^7$
$c_p^{s/l}(T_f - \frac{1}{2}(T_w - T_f)/T_f + \frac{1}{2}(T_0 - T_f))$	1470/4211	$3.374 \cdot 10^7 / 9.666 \cdot 10^7$
$c_p^{s/l}(T_f - \frac{3}{4}(T_w - T_f)/T_f + \frac{3}{4}(T_0 - T_f))$	1172/4209	$2.690 \cdot 10^7 / 9.661 \cdot 10^7$
$c_p^{s/l}(T_w/T_0)$	874/4206	$2.006 \cdot 10^7 / 9.661 \cdot 10^7$

The specific heat of the mushy zone is calculated according to Appendix B.1.

In the lower spatial resolution simulation used, the simulation length is 96 ℓs. Since this is two times lower than the length of the simulation described in table 3.1, all values in LBM-units decrease or increase corresponding to the dimension of ℓs in the unit.

3.8.4. Case 3 - Simulating and Measuring Melting Front in Paraffin
Main Parameters
The third case pertains to a melting front in paraffin. This case is performed both numerically and experimentally. More details about the latter can be found in chapter 4. The parameters used in the numerical enthalpic LBM can be found in tabular 3.5.

Table 3.5: Thermophysical properties used in the numerical model for case 3 in SI- and LBM-units. The origin of the values of L, λ^ϕ and ρ_0 can be found in Appendix B.1

Variable	Description	SI-units	LBM-units
x_{end}	Simulation length	0.1496 m	187 ℓs
T_m	Freezing temperature	327.15 K	273.15 ℓK
T_0	Initial temperature	298.15	298.15 ℓK
T_w	Left wall temperature	363.15 K	363.15 ℓK
L	Latent heat	170 kJ/kg	$3.902 \cdot 10^9$ $\ell s^2/\ell t^2$
$\lambda^{s/l}$	Thermal conductivity	0.22/0.15 W/mK	$0.490/0.334$ $\ell s/\ell t^3 \ell K$
c_p^ϕ	Specific heat	See Table 3.6	$2.295 \cdot 10^{-4} \cdot c_p^\phi$ $\ell s^2/\ell t^2 \ell K$
ρ_0	Density	800 kg/m^3	$1.25 \cdot 10^{-5}$ ℓs^{-3}

Estimate Pairs Specific Heat
The "distance from $T_{f/m}$" and "low-to-high" methods in case 3 do not lead to the same estimate pairs of the temperature-dependent specific heat. Therefore, 10 estimation pairs are evaluated, which can be found in tabular 3.6. The highest 5 estimate pairs are based on the "distance from $T_{f/m}$" method, the following on the "low-to-high" method.

Table 3.6: Definition of the specific heats used in the numerical model for case 3 in SI- and LBM-units. The origin of the values can be found in Appendix B.2

Variable	SI-units (J/kgK)	LBM-units ($\ell s^2/\ell t^2 \ell K$)
$c_p^\phi(T)$	See Appendix B.2	$2.295 \cdot 10^{-4} \cdot c_p^\phi$
$c_p^{s/l}(T_m/T_m)$	2246/2323	$5.156 \cdot 10^7/5.332 \cdot 10^7$
$c_p^{s/l}(T_m - \frac{1}{4}(T_0 - T_m)/T_m + \frac{1}{4}(T_w - T_m)$	2202/2347	$5.056 \cdot 10^7/5.387 \cdot 10^7$
$c_p^{s/l}(T_m - \frac{1}{2}(T_0 - T_m)/T_m + \frac{1}{2}(T_w - T_m)$	2156/2373	$4.949 \cdot 10^7/5.447 \cdot 10^7$
$c_p^{s/l}(T_m - \frac{3}{4}(T_0 - T_m)/T_m + \frac{3}{4}(T_w - T_m)$	2115/2400	$4.855 \cdot 10^7/5.509 \cdot 10^7$
$c_p^{s/l}(T_0/T_w)$	2071/2427	$4.754 \cdot 10^7/5.571 \cdot 10^7$
$c_p^{s/l}(T_0/T_m)$	2071/2323	$4.754 \cdot 10^7/5.332 \cdot 10^7$
$c_p^{s/l}(T_0 + \frac{1}{4}(T_m - T_0)/T_m + \frac{1}{4}(T_w - T_m))$	2115/2347	$4.855 \cdot 10^7/5.387 \cdot 10^7$
$c_p^{s/l}(T_0 + \frac{1}{2}(T_m - T_0)/T_m + \frac{1}{2}(T_w - T_m))$	2156/2373	$4.949 \cdot 10^7/5.447 \cdot 10^7$
$c_p^{s/l}(T_0 + \frac{3}{4}(T_m - T_0)/T_m + \frac{3}{4}(T_w - T_m))$	2202/2400	$5.056 \cdot 10^7/5.509 \cdot 10^7$
$c_p^{s/l}(T_m/T_w)$	2246/2427	$5.156 \cdot 10^7/5.571 \cdot 10^7$

The specific heat of the mushy zone is calculated according to Appendix B.1.

4

Experimental Method

In order to verify the reliability of the proposed numerical solutions based on the enthalpic lattice Boltzmann method, the results should be benchmarked not only by an analytical solution, but by an experiment as well. The material chosen for this experiment is paraffin, as imposing a constant temperature on a wall by heating was much more reliable than by cooling with the available resources. Paraffin has convenient thermophysical properties, since the paraffin used has a phase transition at 327.15 K, which is significantly above room temperature but not much higher. Furthermore, its phases are easily visually distinguished, since its solid phase is opaque and its liquid phase is transparent.

4.1. Experimental Setup

An effort was made to measure a 1D paraffin melting front, insulated perfectly except for a temperature imposing wall, with diffusion through the paraffin solely as heat transporter. The experimental setup is visualized in figure 4.1.

A thin cylindrical glass was used as the base in which a thick layer of paraffin was melted (element 1 in figure 4.1). It is imporant that this glass can withstand temperatures to at least 100^oC for this experiment without breaking or bending. The insulator used was stationary air, which was created by placing the paraffin-filled glass inside a larger cylindrical glass (element 4). The paraffin-filled glass is kept exactly in the middle of the enveloping glass by laser-cutting two wooden pieces with exactly an inner diameter as large as the exterior of the paraffin-filled glass and an outer diameter as large as the interior of the enveloping glass (elements 2). The temperature-imposing wall was placed (partly) inside the paraffin-filled glass, in the form of a hollow cylindrical copper heat transferring element (element 3). This element transfers heat from hot water to the paraffin. This is done by pumping water from a temperature-controlled hot water basin in and out of the element through applied hoses (elements 5). The heating element was made tight-fitting in the paraffin-filled glass, such that the paraffin was heated uniformly.

The setup was placed upright with the heating element on the top, to minimize the convection of liquid paraffin. If heated up, paraffin tends to expand slightly, lowering the density. By placing the heating element on top, the paraffin with the lowest density is automatically at the top. A more detailed list of the materials used can be found in appendix C.1.

4.2. Measurement Procedure

4.2.1. Initialization

The experiment is initiated by setting the temperature of the temperature controlled hot water basin to the desired value, in this experiment 363.15 K. It can be assumed that the temperature decrease in the water due to the heat transfer is neglectible, implying that the temperature of the hot water basin is equal to the wall temperature the heating element imposes on the paraffin. The derivation behind this assumption is given in the appendix C.3.
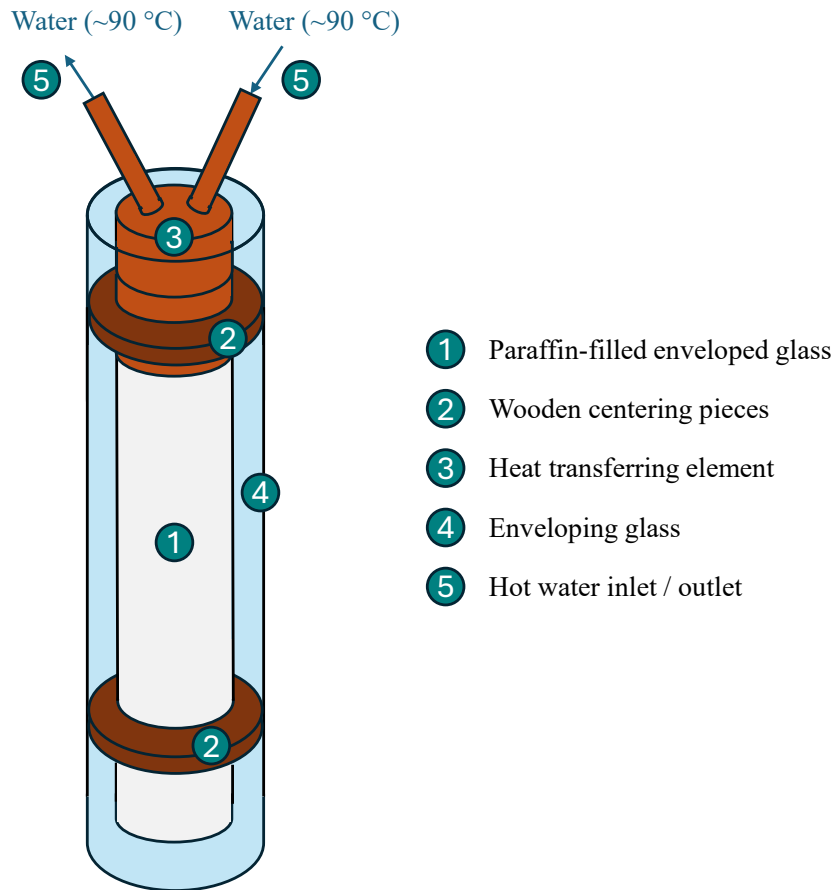
Figure 4.1: The experimental setup

The water is then pumped for several seconds through the heating element before it is put on top of the paraffin. The latter needs to be carried out very securely, in order to prevent the formation of a layer of air between the paraffin and heating element. In this experiment, the heated up heating element was forcefully applied for several seconds to the paraffin layer, in order to melt its very top, which secured a full contact without air bubbles between the heating element and the paraffin layer. The moment the heating element is applied to the paraffin layer, the timing starts.

4.2.2. Data Acquisition
The melting experiment was carried out three times: twice, the melting front propagation was measured until it reached 10 mm, and once, the experiment was carried out for 4.5 hours. The melting front propagation was denoted at least once per 1 mm of propagation, or in the case of a low propagation speed, once every 15 minutes. The melting front propagation was measured from the bottom of the heating element to the border between the opaque and transparent paraffin. This was done by attaching a part of a tape measure to the outside of the paraffin-filled glass to prevent measurement errors due to optical refraction.

<div style="text-align: right; font-size: 3em;">5</div>

Results and Discussion

In order to answer the research questions of this thesis, the enthalpic lattice Boltzmann method discussed in chapter 3 is performed for three cases, described in chapter 3.8. In case 1 and 2, of which the results are shown in chapter 5.1 and 5.2 resp., two freezing problems with different imposed wall temperatures in water are numerically assessed, for multiple spatial resolutions. Case 3, of which the results are shown in chapter 5.3, deals with the melting of paraffin, which is evaluated both numerically and experimentally.

5.1. Simulating Freezing Front in Water - Case 1

5.1.1. Overview Temperature Profile and Front Propagation Implemented Models

In case 1, the heat transfer in water is studied with all six models discussed in chapter 3.7.1, based on the thermophysical properties stated in chapter 3.8.2. The temperature profile and freezing front propagation obtained from the numerical models are shown in figure 5.1.
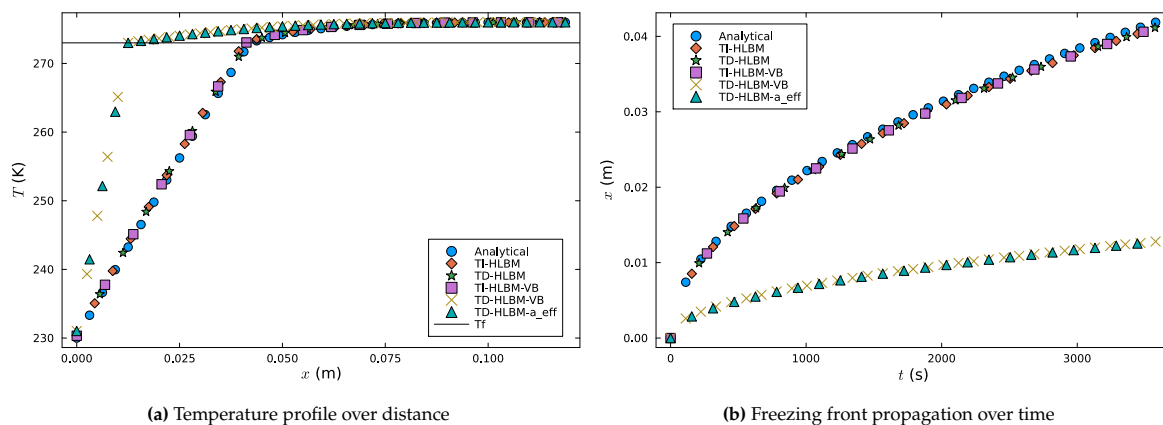

(a) Temperature profile over distance

(b) Freezing front propagation over time

Figure 5.1: Temperature profile and freezing front propagation of water obtained from various numerical models, based on the thermophysical properties in chapter 3.8.2. The models shown have a 192 cell spatial resolution and for the temperature-independent specific heat based models, the $c_p^{s/l}(T_f/T_f)$-pair is used.

As becomes clear, the analytical, TI-HLBM, TD-HLBM and TI-HLBM-VB models show very similar results for both the temperature profile and the freezing front propagation. They collectively show an (almost) linear temperature profile from the wall to the freezing front, which is located at 41.4 mm from the temperature imposed wall after one hour, and a similar curve in the liquid stage.

A similar equality applies to the TD-HLBM-VB and TD-HLBM-a_{eff} models. These models show a similar temperature profile per phase, with the exception that the freezing front has propagated much less far,

<div style="text-align: center;">24</div>

to only around 13.0 mm. Since these two models form no accurate representation of the physical world, the focus is now shifted to the first four models.

5.1.2. Validation of Reliability HLBM models

In order to show the reliability of the implemented models, certain models can be validated by comparing them against each other. The background of this validation is given in section 3.7.2.

1: In order to assess the reliability and the quality of the enthalpic LBM models used, the TI-HLBM model is benchmarked against its analytical solution for both the temperature profile and the freezing front propagation for multiple spatial resolutions. The results are displayed in figure 5.2.
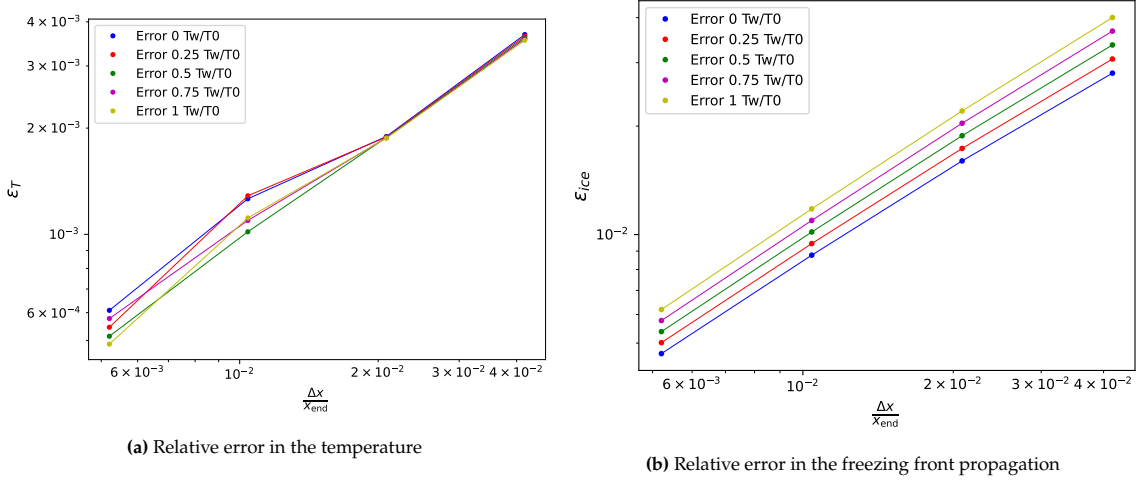

(a) Relative error in the temperature

(b) Relative error in the freezing front propagation

Figure 5.2: Logarithmic plot of the relative error for ice layer thickness and temperature profiles of the constant c_p LBM compared to the analytical solution, as a function of grid resolution $\frac{\Delta x}{x_{end}}$. "Error 0 Tw/T0" denotes the data of estimate $c_p^{s/l}(T_f/T_f)$, "Error 0.25 Tw/T0" denotes $c_p^{s/l}(T_f - \frac{1}{4}(T_w - T_f)/T_f + \frac{1}{4}(T_0 - T_f))$ etc.

This results in average convergence factors for the melting front propagation m and temperature of resp. $m = 0.88 \pm 0.03$ and $n = 0.9 \pm 0.1$.

2: In figure 5.1, it is shown that the TI-HLBM and TI-HLBM-VB model coincide exactly. This was expected, since the Varyazmar and Bazargan model only compensates for an extra term $-T\nabla c_p^{\phi}$, which is zero. This supports the reliability of the Varyazmar and Bazargan based models, since it shows that the models algorithm handles the calculation of ∇c_p^{ϕ} around the propagating front well.

3: As earlier discussed in 5.1.1, the TD-HLBM-VB and TD-HLBM-a$_{eff}$ models show very similar results, which was expected and increases the reliability of the results shown by both models.

5.1.3. Influence Temperature-Independent Estimates

The relative errors of the 96 and 192 cell simulations of the TI-HLBM model to the TD-HLBM model are computed for multiple estimation pairs. The results are shown in figure 5.3.

Temperature Profile

It is shown that the relative error for the temperature profile does not exceed -0.8% and +0.1% for the 96 cell simulation and -0.2% and ~+0.3% for the 192 cell model. The relative error is the highest and shows unstable behavior around the freezing front. In general, the relative error of the temperature-independent specific heat pairs based on the extreme temperatures per phase is the largest.

Front Propagation

The relative error in the freezing front propagation is relatively high in the first seconds of all simulations as a result of the very small freezing front propagation at these instants. After some time, the relative errors converge to a more constant value, with the maximum relative errors of ~-0.13% and 0.29% for

the 96 cell model and -0.13% and 0.35% for the 192 cell model. The relative error for the longer time instances of the specific heat estimate pair based on the wall and initial temperature is the largest. The spikes in the relative error, which point in the direction of the zero relative error axis can be explained by the finite resolution of the model.
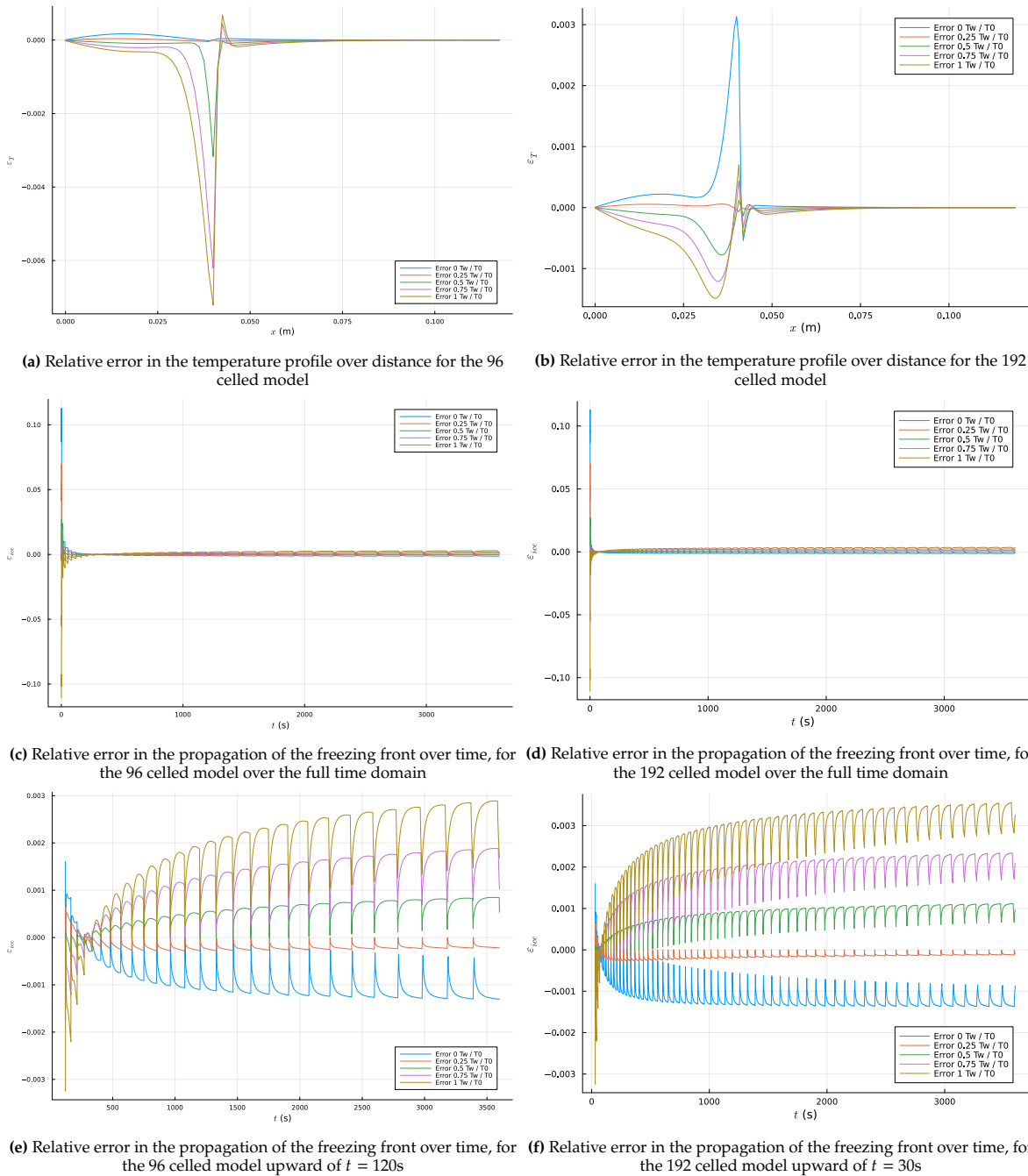

(a) Relative error in the temperature profile over distance for the 96 celled model

(b) Relative error in the temperature profile over distance for the 192 celled model

(c) Relative error in the propagation of the freezing front over time, for the 96 celled model over the full time domain

(d) Relative error in the propagation of the freezing front over time, for the 192 celled model over the full time domain

(e) Relative error in the propagation of the freezing front over time, for the 96 celled model upward of $t = 120s$

(f) Relative error in the propagation of the freezing front over time, for the 192 celled model upward of $t = 30s$

Figure 5.3: Relative errors of numerical solutions of multiple values of the specific heat as an estimate for the temperature-independent specific heat to the temperature-dependent specific heat numerical solution, for two spatial resolutions, based on the thermophysical properties described in chapter 3.8.2. "Error 0 Tw/T0" denotes the data of estimate $c_p^{s/l}(T_f/T_f)$, "Error 0.25 Tw/T0" denotes $c_p^{s/l}(T_f - \frac{1}{4}(T_w - T_f)/T_f + \frac{1}{4}(T_0 - T_f))$ etc.

Most of the time, at least one cell during the HLBM simulation is in phase transition (or: in the mushy zone). For the underestimating specific heat estimate pairs, the spikes correspond to the short period of time in which the TD-HLBM model, against which the relative error is calculated, no cell is in the

mushy zone. This implies that for a short period of time, the freezing front does not propagate in this model, while the TI-HLBM model (which lies behind in the freezing front propagation) can catch up to quickly. However, after another short period of time, another cell in the TD-HLBM model transitions to the mushy phase, and the mushy cell in the TI-HLBM model transitioned fully to the solid phase (no cell is in the mushy zone). This leads to an almost evenly fast increase in the (absolute) relative error.

For the overestimating specific heat estimate pairs, it is the other way around; the spikes correspond to the short period of time in which the freezing front of the TI-HLBM model does not propagate, in which time the TD-HLBM model can catch up with it. Until the TD-HLBM models freezing front propagation 'freezes' and is left behind again.

General Observations

It can be concluded from the graphs that for both spatial resolutions, for both the temperature profile and the freezing front propagation, the $c_p^{s/l}(T_f - \frac{1}{4}(T_w - T_f)/T_f + \frac{1}{4}(T_0 - T_f)$)-pair is the best estimator to let the TI-HLBM model correspond maximally to the TD-HLBM model, since it only very slightly underestimates. The $c_p^{s/l}(T_f - \frac{1}{4}(T_w - T_f)/T_f + \frac{1}{4}(T_0 - T_f)$)-pair is the second best estimator.

The fact that the best estimating pair is not one of the pairs based on the extreme temperatures per phase was expected. However, the estimating pair based on the most central temperatures not being the best estimator is somewhat unexpected.

5.2. Simulating Freezing Front in Water - Case 2

5.2.1. Overview Temperature Profile and Front Propagation Implemented Models

In case 2, again the heat transfer in water is studied with all six models discussed in chapter 3.7.1, based on the thermophysical properties stated in chapter 3.8.3. The case is very similar to case 1, except for a (far) lower left wall temperature T_w. The temperature profile and freezing front propagation obtained from the numerical models are shown in figure 5.4.

(a) Temperature profile over distance

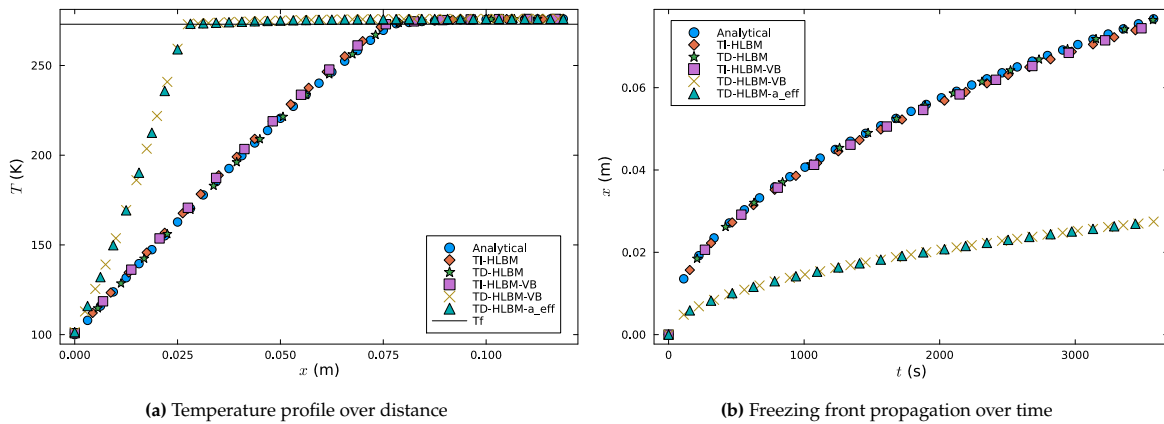**(b)** Freezing front propagation over time

Figure 5.4: Temperature profile and melting front propagation of paraffin obtained from various numerical models, based on the thermophysical properties in chapter 3.8.3. The models shown have a 192 cell spatial resolution and for the temperature-independent specific heat based models, the $c_p^{s/l}(T_f/T_f)$-pair is used.

The analytical, TI-HLBM, TD-HLBM and TI-HLBM-VB models again show very similar results for both the temperature profile and the freezing front propagation. However, a slightly larger difference than in case 1 is observed between the first three mentioned models and the latter. They collectively show an (almost) linear temperature profile from the wall to the freezing front, which is located at 75.7 / 76.9 mm (for the TI- / TD-HLBM model) from the temperature imposing wall after one hour. Furthermore, they show a similar curve in the liquid stage.

Furthermore, the TD-HLBM-VB and TD-HLBM-a_{eff} models again largely coincide, except in the early stages of the freezing front propagation, since the Varyazmar and Bazargan based method needs at least two cells to transition into the solid phase in order to calculate ∇c_p here. They show a somewhat curved

temperature profile in the solid phase, which can be explained by a higher effective thermal diffusivity a_{eff} due to a higher effectivity coefficient β_{eff} for lower temperatures and a higher thermal diffusivity a for lower values of c_p. The freezing front is located at 27.5 mm from the temperature imposing wall after one hour. The curve in the liquid phase is similar to the other models. Since these two models do not form an accurate representation of the physical world, the focus is now shifted to the first four models.

5.2.2. Validation of Reliability HLBM models

In order to show the reliability of the implemented models, certain models can be validated by comparing them against each other. The background of this validation is given in section 3.7.2.

1: In order to assess the reliability and the quality of the enthalpic LBM models used, the TI-HLBM model is benchmarked against its analytical solution for both the temperature profile and the freezing front propagation for multiple spatial resolutions. The results are displayed in figure 5.5.
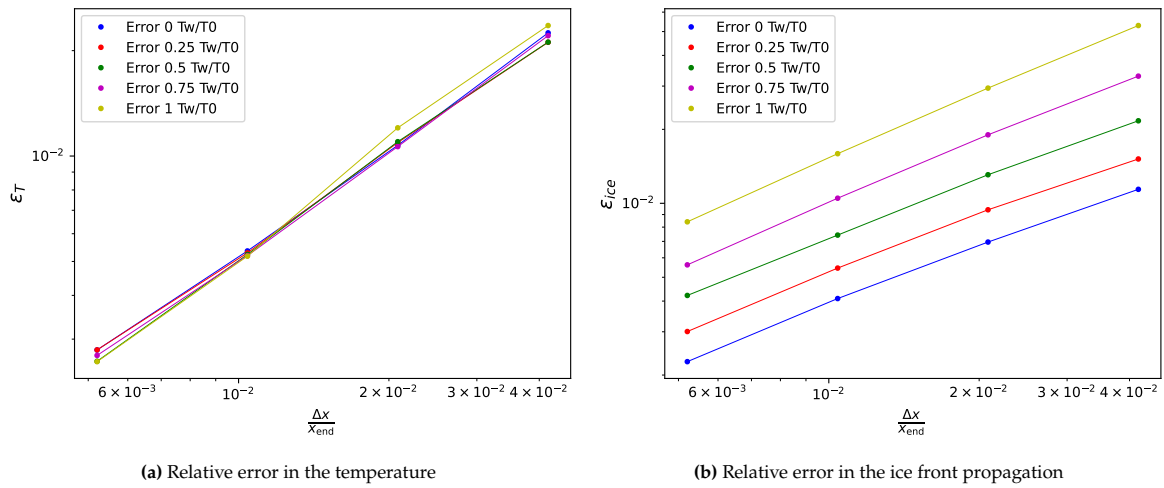
(a) Relative error in the temperature

(b) Relative error in the ice front propagation

Figure 5.5: Logarithmic plot of the relative error for ice layer thickness and temperature profiles of the constant c_p LBM compared to the analytical solution, as a function of grid resolution $\frac{\Delta x}{x_{end}}$. "Error 0 Tw/T0" denotes the data of estimate $c_p^{s/l}(T_f/T_f)$, "Error 0.25 Tw/T0" denotes $c_p^{s/l}(T_f - \frac{1}{4}(T_w - T_f)/T_f + \frac{1}{4}(T_0 - T_f))$ etc.

This results in average convergence factors for the melting front propagation m and temperature of resp. $m = 0.81 \pm 0.04$ and $n = 1.02 \pm 0.05$.

2: In figure 5.4, it is shown that the TI-HLBM and TI-HLBM-VB models coincide exactly, similarly to case 1. This again supports the reliability of this model, as it shows that the model handles the calculation of ∇c_p around the propagating front well.

3: As earlier discussed in 5.2.1, the TD-HLBM-VB and TD-HLBM-a_{eff} models show very similar results, which was expected and again increases the reliability of the results shown by both models.

5.2.3. Influence Temperature-Independent Estimates

The relative errors of the 96 and 192 cell simulations of the TI-HLBM model to the TD-HLBM model are then computed for multiple estimation pairs. The results are shown in figure 5.6.

Temperature Profile

The relative error shown for the temperature profile lies in-between -4.8% and +1.7% for the 96 cell simulation and -4.0% and +1.6% for the 192 cell model. In general, the relative error is the largest in the middle of the solid phase and the temperature profile shows a small degree of unstable behavior around the freezing front. In general, the relative error of the temperature-independent specific heat pairs based on the left wall and initial temperature is the largest (both absolutely and as an underestimator), while the estimation based on the freezing-temperature specific heat is the largest overestimator. However, this estimation has a lower relative error than the two models based on the temperatures closer to the left wall and initial temperature.
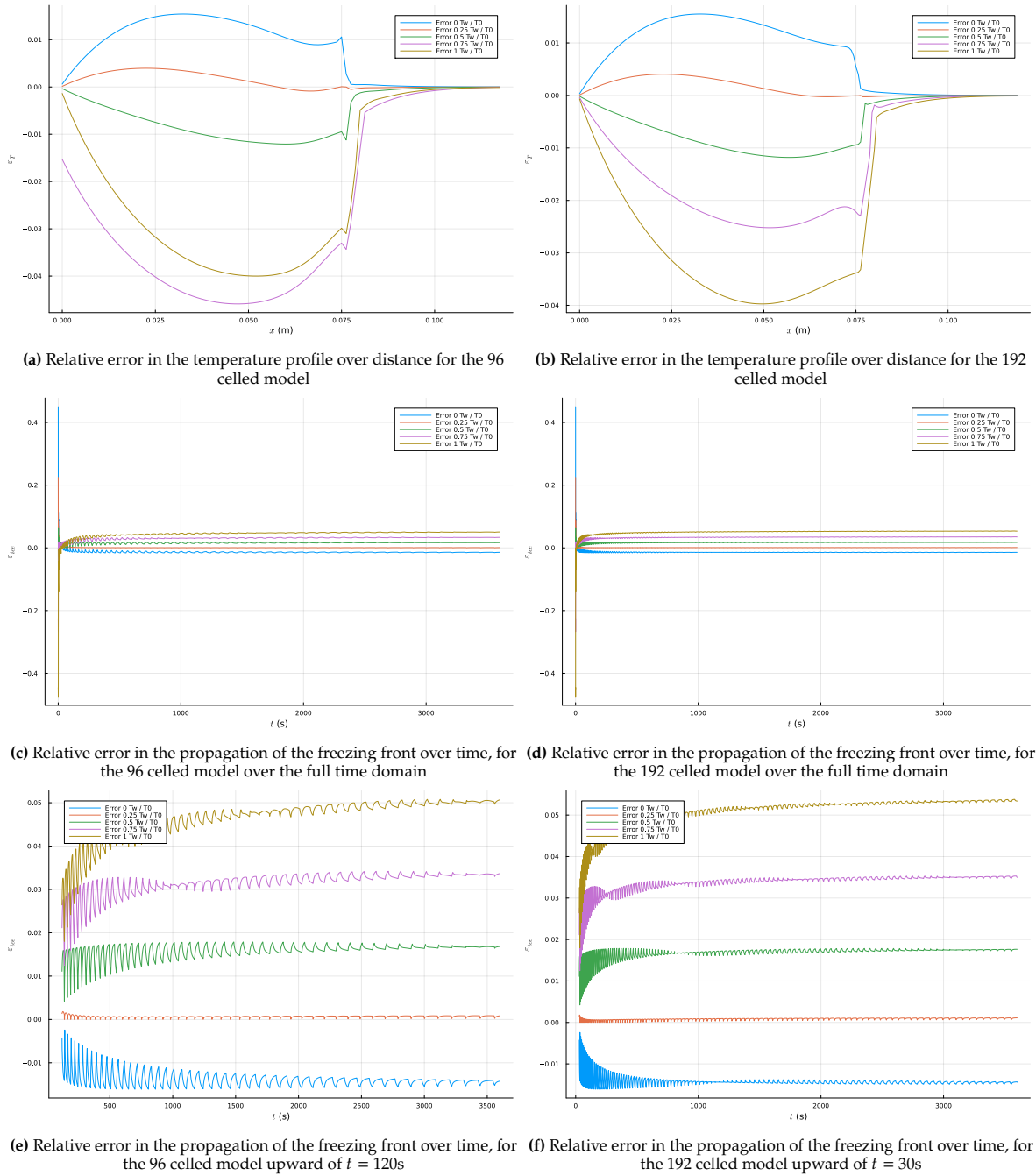
(a) Relative error in the temperature profile over distance for the 96 celled model

(b) Relative error in the temperature profile over distance for the 192 celled model

(c) Relative error in the propagation of the freezing front over time, for the 96 celled model over the full time domain

(d) Relative error in the propagation of the freezing front over time, for the 192 celled model over the full time domain

(e) Relative error in the propagation of the freezing front over time, for the 96 celled model upward of $t = 120s$

(f) Relative error in the propagation of the freezing front over time, for the 192 celled model upward of $t = 30s$

Figure 5.6: Relative errors of numerical solutions of multiple values of the specific heat as an estimate for the temperature-independent specific heat to the temperature-dependent specific heat numerical solution, for two spatial resolutions, based on the thermophysical properties described in chapter 3.8.3. "Error 0 Tw/T0" denotes the data of estimate $c_p^{s/l}(T_f/T_f)$, "Error 0.25 Tw/T0" denotes $c_p^{s/l}(T_f - \frac{1}{4}(T_w - T_f)/T_f + \frac{1}{4}(T_0 - T_f))$ etc.

Front Propagation

The relative error in the freezing front propagation is relatively high in the first seconds of all simulations as a result of the very small freezing front propagation at these instants. After some time, similar to case 1, the relative errors converge to a more constant value, with the maximum relative errors of -1.6% and 5.1% for the 96-cell model and -1.5% and 5.4% for the 192-cell model. The relative error for the longer time instances of the specific heat estimate pair based on the wall and initial temperature is the largest.

The small spikes in the relative error can be explained by the finite resolution of the model. The

explanation for this effect can be found in the results of case 1 (chapter 5.1.3).

The spikes seem smaller for case 2, but this is a deception based on the larger overall relative error. The fact that the spikes seem to disappear for some time in this case is due to the fact that, due to the large relative errors, the overestimators overtake the TD-HLBM models freezing front with more than one cell. This causes a temporary simultaneity in the transition of a cell from the liquid to the mushy phase or from the mushy phase to the solid phase between the two models.

General Observations
It can be concluded from the graphs that for both spatial resolutions, for both the temperature profile and the freezing front propagation, that again the $c_p^{s/l}(T_f - \frac{1}{4}(T_w - T_f)/T_f + \frac{1}{4}(T_0 - T_f)$-pair is the best estimator to let the TI-HLBM model correspond maximally to the TD-HLBM model, where it in this case only slightly overestimates. The $c_p^{s/l}(T_f - \frac{1}{2}(T_w - T_f)/T_f + \frac{1}{2}(T_0 - T_f)$-pair is again the (shared) second best estimator, along with the $c_p^{s/l}(T_f/T_f)$-pair. The correlation to case 1 leads to an interesting insight in that, for freezing problems in water with the used dependency of the specific heat on temperature (see app. B.1.1), the $c_p^{s/l}(T_f - \frac{1}{4}(T_w - T_f)/T_f + \frac{1}{4}(T_0 - T_f)$-pair is the universal best estimator.

Furthermore, case 1 and 2 collectively form a conclusion about the effect of a lower wall temperature and lower spatial resolution on the relative error. It is found that spatial resolution has no significant influence on the most important and stable relative error: that of the ice front propagation. This supports a conclusion that it is likely that in general, for resolutions which accurately correspond to their analytical solution, there is no relation between the spatial resolution of the model. However, this conclusion can not fully be drawn, due to the low amount of cases researched.

It is, however, very likely that it can be generalized that for an increase in the temperature difference between the freezing/melting temperature and the extreme temperatures per phase (the wall temperature and the initial temperature), the relative error of the estimates increase for specific heats that (about) linearly depend on temperature. The change in relative error is such significant, that this result is very likely generalizable. Compare for instance the relative errors for $c_p^{s/l}(T_f/T_f)$ for case 1 and 2. The values of c_p^{ϕ} coincide, but the relative ice front errors after some time are resp. 0.13% and 1.3%.

5.3. Simulating and Measuring Melting Front in Paraffin - Case 3

In case 3, heat transfer in the form of a melting front in paraffin is studied, based on the thermophysical properties stated in chapter 3.8.4. Since not only numerical results, but also experimental solutions for this heat problem are given, the focus lies purely on the numerical methods that (try to) represent physical reality. These will be described first, which will be followed by the section in which the experiments will be compared to the numerical models.

5.3.1. Numerical Assessment
Overview Temperature Profile and Front Propagation Implemented Models
In case 3, only the TI- and TD-HLBM models are considered, alongside the analytical solution to benchmark these models. The temperature profile and freezing front propagation obtained from the numerical models are shown in 5.7.
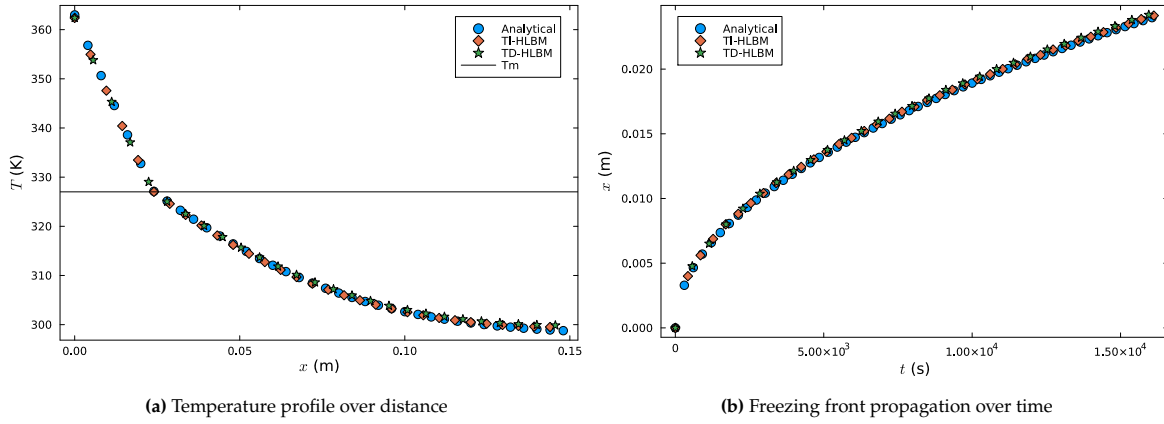
(a) Temperature profile over distance

(b) Freezing front propagation over time

Figure 5.7: Temperature profile and melting front propagation of paraffin obtained from various numerical models, based on the thermophysical properties in chapter 3.8.4. For the temperature-independent specific heat based models, the $c_p^{s/l}(T_f/T_f)$-pair is used.

The analytical solution and the TI- and TD-HLBM models again show very similar results for both the temperature profile and the freezing front propagation. Only a slight difference between all is observed. However, they still collectively show an (almost) linear temperature profile from the wall to the melting front, which is located at 24.1 / 24.3 mm (for the TI- / TD-HLBM model) from the temperature imposing wall after 4.5 hours. Furthermore, they show a similar curve in the solid stage.

Influence Temperature-Independent Estimates
The relative errors for the simulations of the TI-HLBM model to the TD-HLBM model are then computed for multiple estimation pairs. The results are shown in figure 5.8.

Temperature Profile

The relative error shown for the temperature profile lies in-between -0.16% and +0.07% for the simulation with specific heat estimates which originate from the "distance from $T_{f/m}$"-method. For the estimates based on the 'low to high'-method, the relative error lies in-between the same values and is almost indistinguishable to the "distance from $T_{f/m}$"-method estimates.

However, the order of the lines is of great interest. The lines with the same estimation for the liquid temperature-independent heat c_p^l almost coincide, while the order of the lines with the same estimation for the solid temperature-independent heat c_p^s is turned upside-down. It is shown that the estimations for the temperature profile with a certain estimation for the liquid temperature-independent heat c_p^l have a lower relative error in the liquid phase in combination with an estimated solid specific heat, if the two are related by having the same ratio from the melting temperature towards the extreme temperature of their phase ("distance from $T_{f/m}$"-ratio), in reference to the same "low to high"-ratio. The relative errors for the solid phase do almost perfectly coincide for both methods in determining the best estimate pair.

Front Propagation

The relative error in the freezing front propagation is again relatively high in the first seconds of all simulations as a result of the very small freezing front propagation at these instants. After some time, the relative errors converge to a more constant value, with the maximum relative errors of -0.9% and 0.7% for the "distance from $T_{f/m}$"-method specific heat estimate pair and -1.2% and 0.9% for the 'low to high'-method estimate pair.

The relative error in the melting front propagation shows a similar pattern to the temperature profile, with the relative errors for the estimate pairs with the same estimate for the c_p^l being almost similar of form, except for a slightly larger error for the estimate pair with the same 'low to high'-ratio. The small spikes in the relative error can, similar to case 1 and 2, be explained by the finite resolution of the model. The explanation for this effect can be found in the results of case 1 (chapter 5.1.3).
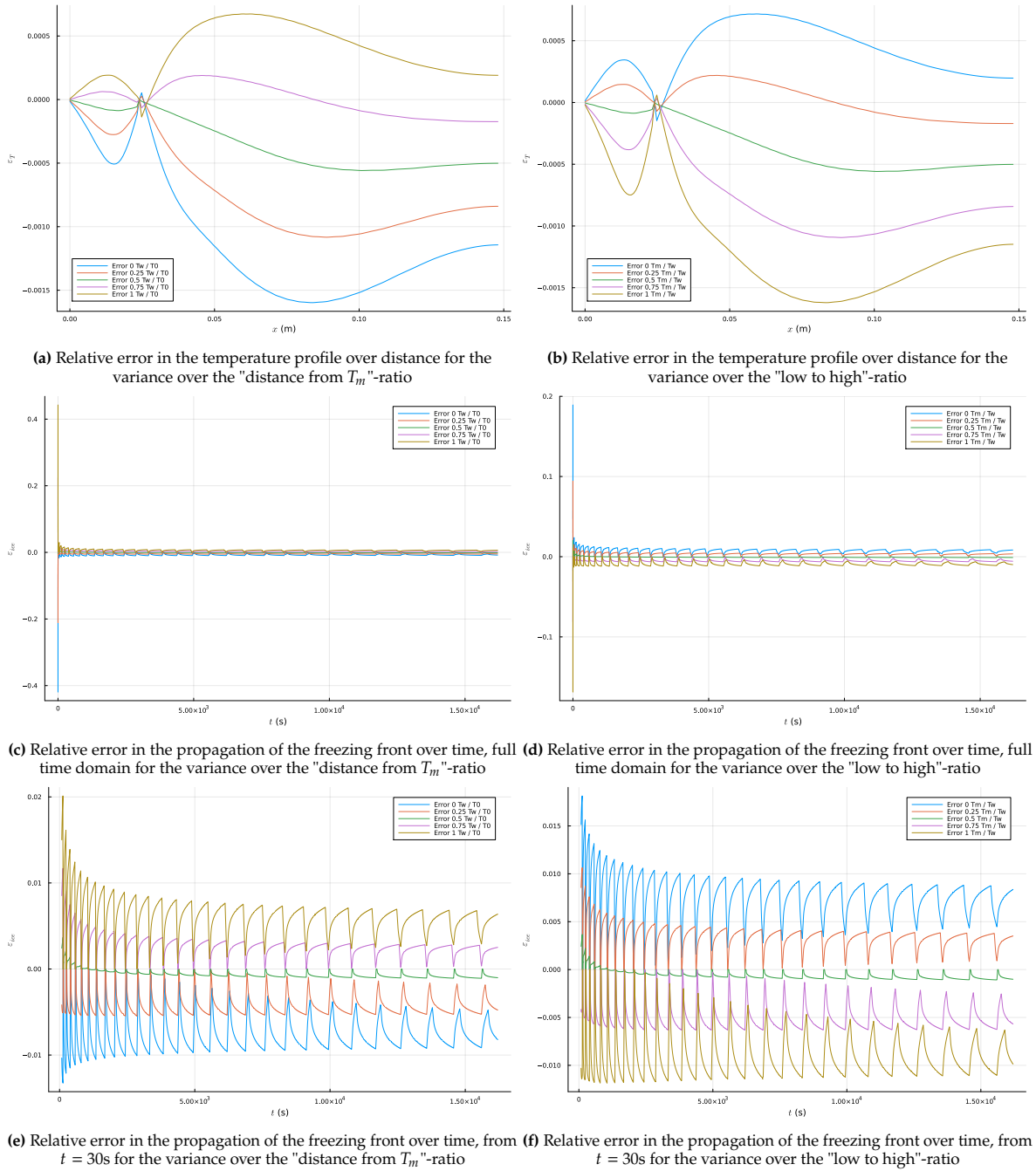
(a) Relative error in the temperature profile over distance for the variance over the "distance from T_m"-ratio

(b) Relative error in the temperature profile over distance for the variance over the "low to high"-ratio

(c) Relative error in the propagation of the freezing front over time, full time domain for the variance over the "distance from T_m"-ratio

(d) Relative error in the propagation of the freezing front over time, full time domain for the variance over the "low to high"-ratio

(e) Relative error in the propagation of the freezing front over time, from $t = 30$s for the variance over the "distance from T_m"-ratio

(f) Relative error in the propagation of the freezing front over time, from $t = 30$s for the variance over the "low to high"-ratio

Figure 5.8: Relative errors of numerical solutions of multiple values of the specific heat as an estimate for the temperature-independent specific heat to the temperature-dependent specific heat numerical solution, based on the thermophysical properties described in chapter 3.8.4. "Error 0 Tw/T0" denotes the data of estimate $c_p^{s/l}(T_f/T_f)$, "Error 0.25 Tw/T0" denotes $c_p^{s/l}(T_f - \frac{1}{4}(T_w - T_f)/T_f + \frac{1}{4}(T_0 - T_f))$ "Error 0.25 Tm/T0" denotes $c_p^{s/l}(T_0 - \frac{1}{4}(T_m - T_0)/T_m + \frac{1}{4}(T_w - T_m))$ etc.

General Observations

To conclude, this could imply that for the specific heat of paraffin used in this thesis and for melting problems, the estimate for the liquid specific heat c_p^l is dominant in determining the relative error to the TD-HLBM model. The combination with the estimate for the solid specific heat c_p^s determines if the relative error comes out somewhat higher or lower in both the temperature profile in the liquid phase as in the melting front propagation. The "distance from $T_{f/m}$"-method is then the method with the lowest relative error for its estimate pairs.

The best estimate for the paraffin is equal for both methods to form specific heat estimation pairs, since this pair is equal for both: the $c_p^{s/l}(T_f - \frac{1}{2}(T_w - T_f)/T_f + \frac{1}{2}(T_0 - T_f) = c_p^{s/l}(T_0 - \frac{1}{2}(T_m - T_0)/T_m + \frac{1}{2}(T_w - T_m)$-pair, which slightly underestimates the temperature profile and the melting front propagation.

5.3.2. Experimental Assessment

Overview Measurements vs. TD-HLBM model

Three experiments were carried out, which are described in chapter 4. The measurements are plotted in figure 5.9, together with the TD-HLBM model shown in section 5.3.1 which should represent the outcome of the measurements in perfect insulating conditions.
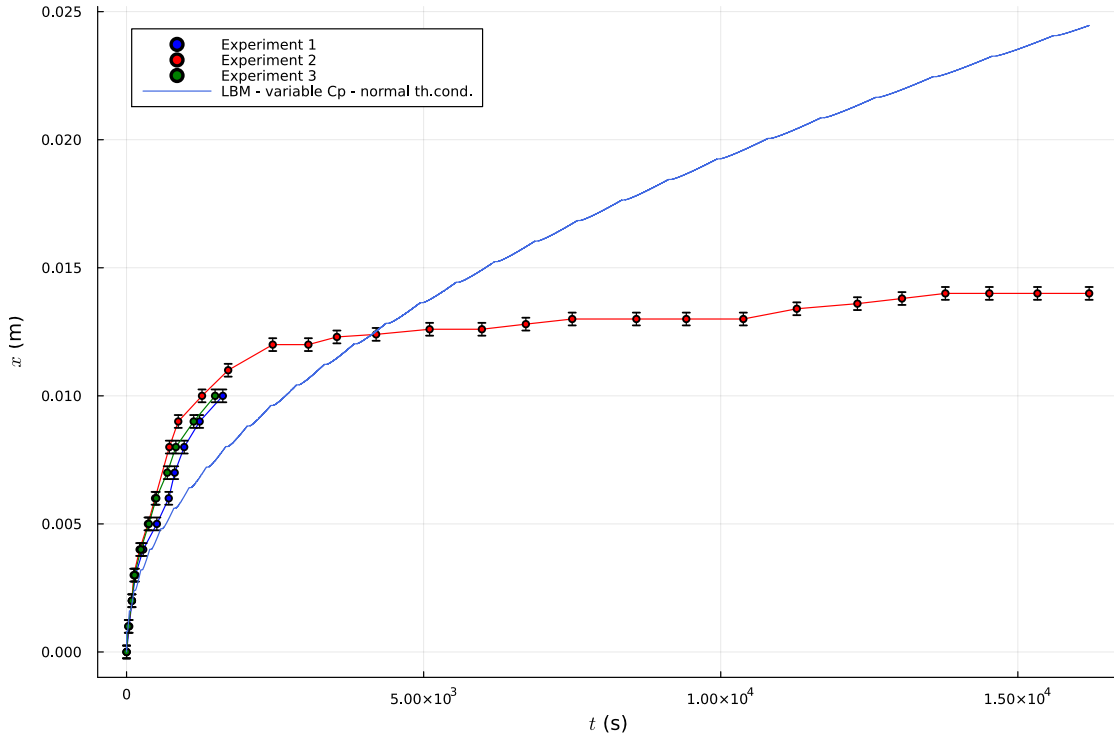
Figure 5.9: Melting front propagation over time of paraffin after $t = 16200$s, obtained from the TD-HLBM model, based on the thermophysical properties in chapter 3.8.4, and experimental measurements

As shown, the values do not coincide with the model. For small values, the melting front propagation is underestimated by the model, while around 12.5 mm the propagation is overestimated. It seems like the experimentally determined melting front propagation has a maximum value of around 14.0 mm.

Discussion Overview Measurements vs. TD-HLBM model

The deviation of the experimental values from the model can be explained by considering an additional path of heat transportation for the paraffin and by considering heat losses. The enveloped glass, which is filled with paraffin, can transport the heat from the heating element to the paraffin as well. This plays a significant role, since the thermal conductivity of glass is high compared to that of liquid paraffin: $\lambda_{\text{glass}} = 1.05$ W/mK [27], $\lambda_{\text{paraffin}}^l = 0.15$ W/mK.

Additionally, however large efforts were made to reduce the heat losses, heat was still lost due to radiation and heat diffusion through the insulation layer.

The estimates for the additional heat sources and heat losses are quantified, along the transport of heat through the paraffin itself, and are shown in figure 5.10. The origin and reasoning behind the values shown can be found in appendix C.2.
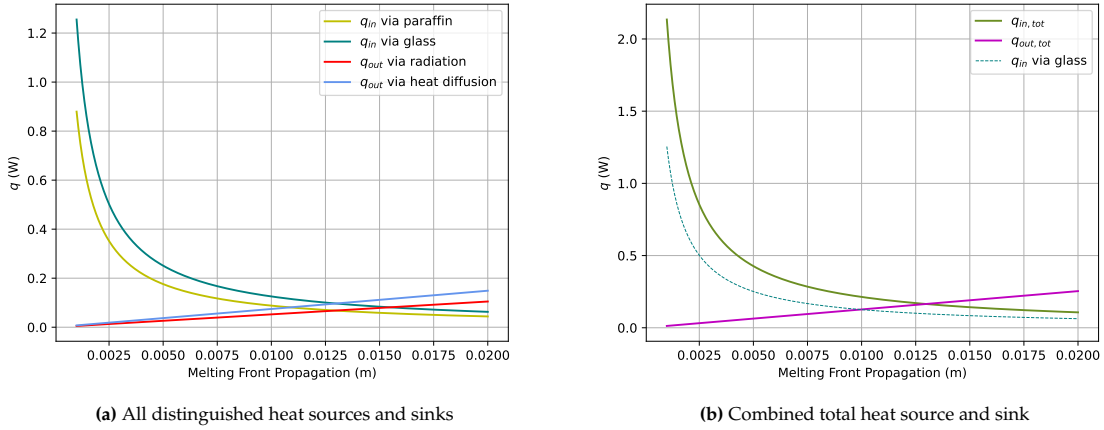
(a) All distinguished heat sources and sinks

(b) Combined total heat source and sink

Figure 5.10: Heat sources and sinks which play a significant role in the paraffin melting front experiment

In figure 5.10b it can be found that for the first 5 millimeters of the melting front propagation, the heat loss is almost negligible in comparison to the incoming heat in the paraffin. Therefore, the experimental measurements for that region should match an enthalpic paraffin model with the incoming heat through the paraffin itself and the glass it is in. In order to simulate this model, the effective thermal conductivity of the paraffin λ^{ϕ}_{eff} was set up (see eq. C.1).

Furthermore, it can be found in figure 5.10b that at 10.0 mm propagation, it is estimated that the heat loss is equal to the incoming heat through the glass, resulting in an effective heat inlet which is what it would be in the case of the enthalpic LBM model for paraffin with 'normal' thermal conductivities, for a melting front propagation of this distance. This implies that the curvature (most importantly, the slope) of the line connecting the experimental measurements around a melting front propagation of 10 mm should match that of the 'normal' thermal conductivity enthalpic method shown in figure 5.9 around the same melting front propagation.

With these two points of discussion on mind, the experimental measurements are plotted again for the first hour, together with the enthalpic LBM models for paraffin with one using the 'normal' thermal conductivities and the other the effective thermal conductivities. This is shown in figure 5.11.

It is shown that the measurements indeed follow the LBM with the effective thermal conductivity quite well for the first several millimeters of the melting front propagation. The coincidence is not perfect; this can be explained by the fact that in the early stage of the experiment, a large part of the heat that is transported through the glass is used not only for the heating of the paraffin, but also for the heating of the glass itself. Furthermore, it can be concluded from the figure that the slope of the line drawn between the experimental measurements around x = 10 mm matches the slope of the numerical model with the normal thermal conductivity at x = 10 mm quite well.

Finally, from figure 5.10b it can be concluded that the heat inflow matches the heat outflow around a 13 mm melting front propagation, which should result in a standstill of the melting front at this value. Although the maximum value measured was 14 mm, which implies that the heat inflow and outflow estimations made do not perfectly match reality, this forms an explanation for the stagnation of the melting front around 14 mm.
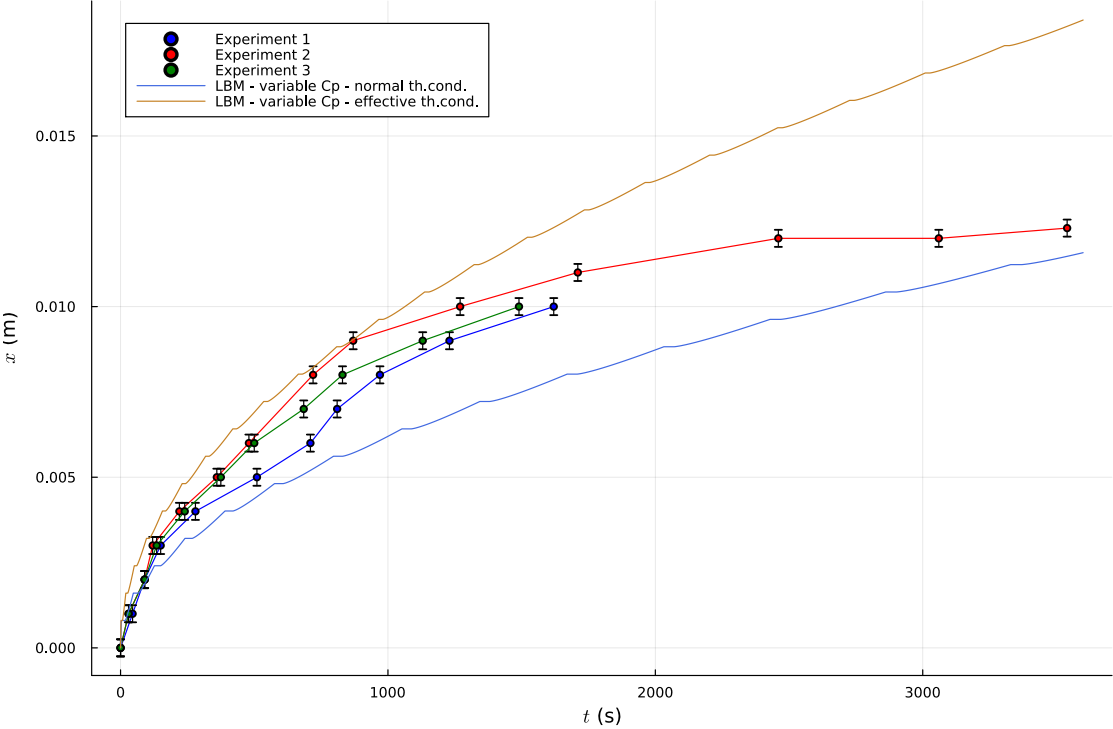
Figure 5.11: Melting front propagation over time of paraffin after $t = 3600s$, obtained from two TD-HLBM models, with one using 'normal' values of the thermal conductivity (see chapter 3.8.4) and the other an effective thermal conductivity, and experimental measurements

6

Conclusion and Recommendations

Nuclear reactors are essential to achieve a reliable and carbon-neutral energy supply. Molten Salt Fast Reactors form a promising alternative for conventional nuclear reactors. In the electricity generating process, the energy of radioactive radiation is converted into electricity via multiple stages of heat transfer. The numerical computation of this heat transfer is an essential key in our understanding of this heat transfer. A widely used method to model heat transfer problems is the enthalpic lattice Boltzmann method (HLBM). In order to make this enthalpic LBM as reliable and close to reality as possible, this study examined the effect of the assumption of a temperature-independent specific heat in this numerical computation. This was specifically done for cases where a phase transition occurs in the heat transfer process.

Three cases were analyzed. In the first two, the propagation of a mobile freezing front in water for different imposed wall temperatures was investigated by numerical computation. The deviation between the model based on a temperature-independent and -dependent specific heat (resp. TI-HLBM and TD-HLBM model) in these cases remained small; even for the worst reasonable approximation of the specific heat, for a large temperature difference between the temperature imposed wall and the freezing temperature, the relative error for the temperature profile and the freezing front propagation obtained an absolute maximum of resp. -4.8% and 5.4%. For a smaller difference between these temperatures, this maximum absolute relative error was resp. -0.8% and +0.35%.

The relative error of the TI-HLBM model compared to the TD-HLBM model increased for an increasing temperature gap between the temperature-imposed wall and the melting temperature for water. The relative error remained however within acceptable bounds. It could furthermore be found that for a model with a lower spatial resolution, similar dependencies were found of the relative error on the solid-liquid temperature-independent specific heat pair, implying that the findings for one spatial resolution might be extended to other resolutions.

The third case involved the propagation of a mobile melting front in paraffin, which was investigated by using both a numerical computation and experimental measurements. The deviation between the TI- and TD-HLBM models in this cases was, similar to the first two cases, not significantly large, and remained within an absolute maximum of -0.16% and -1.2% for resp. the temperature profile and melting front propagation.

The most accurate way to imitate the TD-HLBM model for paraffin was by using a solid-liquid temperature-independent specific heat pair which are, similar to the first two cases, based on the temperature-dependent relation for specific heat, for temperatures which have a similar ratio of being halfway from the melting temperature T_m towards the extreme temperature of the phase: the initial temperature T_w for the liquid phase and the imposed temperature on the wall T_w for the solid phase ("distance from $T_{f/m}$"-ratio). This can be denoted by $c_p^{s/l}(T_m - \frac{1}{2}(T_0 - T_f)/T_m + \frac{1}{2}(T_w - T_m))$. For water, this value was found a quarter in this same way, for $c_p^{s/l}(T_f - \frac{1}{4}(T_w - T_f)/T_f + \frac{1}{4}(T_0 - T_f))$.

Furthermore, parallels could be drawn between the TD-HLBM model and the experimental measure-

ments, if the additional heat transfer by the glass and the heat losses by radiation and heat diffusion are taken into account.

6.1. Conclusion

In general, it can be concluded that assuming a temperature-independent specific heat has a small effect on the results of an enthalpic LBM-based numerical simulation for the heat transfer problems in water and paraffin researched; the relative error for all cases researched is lower than 5.4%. This result can, with great certainty, be expanded to other systems with an (mostly) linear dependence of the specific heat on the temperature, for initial and wall temperatures not too highly deviating from the melting/freezing temperature. The relative error of assuming a temperature-independent specific heat increases as the difference increases between the initial or wall temperature and the melting/freezing temperature. The relative error does not vary much for a lower spatial resolution, although this is not investigated thoroughly.

The most simple, efficient and accurate lattice Boltzmann method scheme to incorporate the effect of a temperature-dependent specific heat is the TD-HLBM model. But if a temperature-independent specific heat is considered, for an unknown system, the most safe guess for the, in general, lowest relative error is with great certainty the solid-liquid temperature-independent specific heat pair which are based on the temperature-dependent relation for specific heat, for temperatures which have a similar ratio of being halfway from the melting/freezing temperature $T_{m/f}$ towards the extreme temperature of the phase, the initial and wall temperature T_0/T_w.

However, for simulating a freezing problem in water, the optimal solid-liquid temperature-independent specific heat pair was found to be a quarter of the way from the melting/freezing temperature $T_{m/f}$ towards the extreme temperature of the phase, the initial temperature and wall temperature T_0/T_w.

Some of the proposed LBM schemes which incorporate the effect of a temperature-dependent specific heat reflect the physical reality. The TD-HLBM-VB and TD-HLBM-a$_{\text{eff}}$ models do not reflect a physical reality, since in the physical foundation of these models a large approximation error is made. The analytical solution and the TI-HLBM, TD-HLBM and TI-HLBM-VB models do, very likely, all reflect reality. However, when using these LBM schemes, it is important to consider all sources of heat sources and sinks to parallelize them to the physical world.

6.2. Recommendations

Based on the findings of this thesis, several directions for future research can be proposed.

This research has focused the heat exchange in two materials: paraffin and water, with both (almost) linear dependence of the specific heat on temperature. In further research, the effect of considering a temperature-independent specific heat while the actual dependency of temperature is nonlinear is advised. More research needs to be conducted to verify the statements about the dependencies of the relative error on the spatial resolution and the temperature difference between the melting/freezing temperature and the initial and wall temperature.

Furthermore, additional research needs to be conducted to find an explanation for or any form of logic behind the value of the best-imitating temperature-independent specific heat pair, such that a method can be set up such that the optimal values can easily be found for any material.

Lastly, in this thesis, only the effect of assuming a constant specific heat is investigated. The thermal conductivity is highly dependent on the temperature as well. How big is the influence of using a temperature-independent thermal conductivity in this thesis on the results of the numerical outcome of both the TI- and TD-HLBM models? And in the theory, the term $\nabla \rho^{\phi}$ was approximated to zero. What is the effect on the solutions if this can not be done? Can a lattice Boltzmann method based model be proposed in order to solve this enthalpy equation?

References

[1]   M. Allibert et al. "7 - Molten salt fast reactors". In: *Handbook of Generation IV Nuclear Reactors*. Ed. by Igor L. Pioro. Woodhead Publishing Series in Energy. Woodhead Publishing, 2016, pp. 157–188. ISBN: 978-0-08-100149-3. DOI: `https://doi.org/10.1016/B978-0-08-100149-3.00007-0`.

[2]   R.J.L. Andon and J.F. Martin. "Thermodynamic properties of hexacosane". In: *The Journal of Chemical Thermodynamics* 8.12 (1976), pp. 1159–1166.

[3]   B.W. Ang, P. Zhou, and L.P. Tay. "Potential for reducing global carbon emissions from electricity production—A benchmarking analysis". In: *Energy Policy* 39.5 (2011), pp. 2482–2489.

[4]   C.M.L. Atkinson, J.A. Larkin, and M.J. Richardson. "Enthalpy changes in molten n-alkanes and polyethylene". In: *The Journal of Chemical Thermodynamics* 1.5 (1969), pp. 435–440.

[5]   C. Bus. "Simulating the Transient Freezing in cooled Non-eutectic Molten Salt Channel Flow". MA thesis. Delft University of Technology, 2022.

[6]   C. Bus, T.Besseling, and M. Rohde. "A Filter-Matrix Lattice-Boltzmann Methodology for Convective Melting and Solidification". In: *International Journal for Numerical Methods in Fluids* (2025). DOI: `https://doi.org/10.1002/fld.70001`.

[7]   S. Chen, B. Yang, and C. Zheng. "A lattice Boltzmann model for heat transfer in heterogeneous media". In: *International Journal of Heat and Mass Transfer* 102 (2016), pp. 637–644.

[8]   G. de Fabritiis et al. "Mesoscopic Models of Liquid/Solid Phase Transitions". In: *International Journal of Modern Physics C* 09.08 (1998), pp. 1405–1415. DOI: `10.1142/S0129183198001278`.

[9]   S. Fukusako. "Thermophysical properties of ice, snow, and sea ice". In: *International Journal of Thermophysics* 11 (1990), pp. 353–372.

[10]   *Fysische Transportverschijnselen: Denken in Balansen | TU Delft OPEN Books — doi.org*. `https://doi.org/10.5074/t.2023.002`. [Accessed 04-06-2025].

[11]   N. Gupta, G.R. Chaitanya, and S.C. Mishra. "Lattice Boltzmann method applied to variable thermal conductivity conduction and radiation problems". In: *Journal of Thermophysics and Heat Transfer* 20.4 (2006), pp. 895–902.

[12]   R. Hamila et al. "Lattice Boltzmann method for heat transfer problems with variable thermal conductivity". In: *International Journal of Heat and Technology* 35.2 (2017), pp. 313–324.

[13]   A. Ho et al. "Exploring the benefits of molten salt reactors: An analysis of flexibility and safety features using dynamic simulation". In: *Digital Chemical Engineering* 7 (2023), p. 100091. ISSN: 2772-5081. DOI: `https://doi.org/10.1016/j.dche.2023.100091`.

[14]   R. Huang, H. Wu, and P. Cheng. "A new lattice Boltzmann model for solid–liquid phase change". In: *International Journal of Heat and Mass Transfer* 59 (2013), pp. 295–301.

[15]   H. Inaba and P. Tu. "Evaluation of thermophysical characteristics on shape-stabilized paraffin as a solid-liquid phase change material". In: *Heat and Mass Transfer* 32.4 (1997), pp. 307–312.

[16]   W.-S. Jiaung, J.-R. Ho, and C.-P. Kuo. "Lattice Boltzmann method for the heat conduction problem with phase change". In: *Numerical Heat Transfer: Part B: Fundamentals* 39.2 (2001), pp. 167–187.

[17]   Y. Jin and B. Wunderlich. "Heat capacities of paraffins and polyethylene". In: *The Journal of Physical Chemistry* 95.22 (1991), pp. 9000–9007.

[18]   M.M. Kenisarin. "Thermophysical properties of some organic phase change materials for latent heat storage. A review". In: *Solar Energy* 107 (2014), pp. 553–575. ISSN: 0038-092X. DOI: `https://doi.org/10.1016/j.solener.2014.05.001`. URL: `https://www.sciencedirect.com/science/article/pii/S0038092X14002291`.

[19]   M. Kraiem et al. "Thermophysical characterization of paraffins versus temperature for thermal energy storage". In: *Buildings* 13.4 (2023), p. 877.

[20]   T. Krüger et al. *The Lattice Boltzmann Method: Principles and Practice*. Springer International Publishing AG Switzerland, 2017.

[21]   D. LeBlanc. "Molten salt reactors: A new beginning for an old idea". In: *Nuclear Engineering and Design* 240.6 (2010), pp. 1644–1656. ISSN: 0029-5493. DOI: https://doi.org/10.1016/j.nucengdes.2009.12.033.

[22]   Z. Li and E. Gariboldi. "Review on the temperature-dependent thermophysical properties of liquid paraffins and composite phase change materials with metallic porous structures". In: *Materials Today Energy* 20 (2021), p. 100642.

[23]   S.C. Mishra et al. "Combined conduction and radiation heat transfer with variable thermal conductivity and variable refractive index". In: *International Journal of Heat and Mass Transfer* 51.1-2 (2008), pp. 83–90.

[24]   C.O. Popiel and J. Wojtkowiak. "Simple formulas for thermophysical properties of liquid water for heat transfer calculations (from 0 C to 150 C)". In: *Heat transfer engineering* 19.3 (1998), pp. 87–101.

[25]   E. H. Ratcliffe. "The thermal conductivity of ice new data on the temperature coefficient". In: *The Philosophical Magazine: A Journal of Theoretical Experimental and Applied Physics* 7.79 (1962), pp. 1197–1203. DOI: 10.1080/14786436208209120.

[26]   M. Rohde. "Nuclear Reactor Thermal Hydraulics (AP3641)". Reader of course AP3641 at Delft University of Technology. 2014.

[27]   *The Engineering ToolBox — engineeringtoolbox.com*. https://www.engineeringtoolbox.com/. [Accessed 24-06-2025].

[28]   N. Ukrainczyk, S. Kurajica, and J. Šipušić. "Thermophysical comparison of five commercial paraffin waxes as latent heat storage materials". In: *Chemical and biochemical engineering quarterly* 24.2 (2010), pp. 129–137.

[29]   M. Varmazyar and M. Bazargan. "Development of a thermal lattice Boltzmann method to simulate heat transfer problems with variable thermal conductivity". In: *International Journal of Heat and Mass Transfer* 59 (2013), pp. 363–371.

[30]   D.V. Widder. *The heat equation*. Vol. 67. Academic Press, 1976.

[31]   D. Wolf-Gladrow. "A lattice Boltzmann equation for diffusion". In: *Journal of statistical physics* 79 (1995), pp. 1023–1032.

<div align="right">

A

</div>
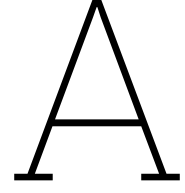
∇c_p calculating algorithm

A.1. First Order Accurate algorithm

First, some or all of the vector components of ∇c_p are set to 0 for the few cells for which ∇c_p is indeed 0 (first point below) or cannot be calculated (second and third point below). This is the case for the following cells:

- For cells in the mushy phase in case of a chemically pure substance, since $\nabla T = \vec{0}$ in this phase, $\nabla c_p = \vec{0}$

- For cells at the model boundary in the case that the neighboring cell opposite to the boundary is in a different phase, the component of ∇c_p perpendicular to the boundary should be set to 0

- For cells that are enclosed by two neighboring cells on opposite sides with both a different phase to the enclosed cell, the component of ∇c_p in the direction of those two cells should be set to 0.

Secondly, for some specific cells states below, the following method is used to calculate ∇c_p:

$$\nabla c_p(\vec{x}, t)_{\vec{r}} = \frac{c_p(\vec{x}, t) - c_p(\vec{x} - \vec{r}\Delta x, t)}{\Delta x} + O(\Delta x) \tag{A.1}$$

in which $\vec{r}$ is a normalized direction vector. This method is used for the following cells:

- For cells whose neighbor in the $\vec{r}$-direction is a model boundary in the case that the second cell in the direction opposite to the boundary is in a different phase, the component of ∇c_p in the $\vec{r}$-direction is calculated by eq. A.1

- For cells for which the neighboring cell in the $\vec{r}$-direction is in a different phase and the second cell in the $-\vec{r}$ direction is in a different phase as well, or is over the boundary, the component of ∇c_p in the $\vec{r}$ direction of those two cells should be calculated by eq. A.1.

Thirdly, for some specific cells states below, the following method is used to calculate ∇c_p:

$$\nabla c_p(\vec{x}, t)_{\vec{r}} = \frac{3c_p(\vec{x}, t) - 4c_p(\vec{x} - \vec{r}\Delta x, t) + c_p(\vec{x} - 2\vec{r}\Delta x, t)}{2\Delta x} + O(\Delta x^2) \tag{A.2}$$

in which $\vec{r}$ is a normalized direction vector. This method is used for the following cells:

- For cells whose neighbor in the $\vec{r}$-direction is a model boundary or has a different phase, the component of ∇c_p in the $\vec{r}$-direction is calculated by eq. A.2

Fourthly, for some specific cells states below, the following method is used to calculate ∇c_p:

$$\nabla c_p(\vec{x}, t)_{\vec{r}} = \frac{c_p(\vec{x} + \vec{r}\Delta x, t) - c_p(\vec{x}, t)}{\Delta x} + O(\Delta x) \tag{A.3}$$

in which $\vec{r}$ is a normalized direction vector. This method is used for the following cells:

- For cells whose neighbor in the $-\vec{r}$-direction is a model boundary in the case that the second cell in the direction opposite to the boundary is in a different phase, the component of ∇c_p in the $\vec{r}$-direction is calculated by eq. A.3

- For cells for which the neighboring cell in the $-\vec{r}$-direction is in a different phase and the second cell in the $\vec{r}$ direction is in a different phase as well, or is over the boundary, the component of ∇c_p in the $\vec{r}$ direction of those two cells should be calculated by eq. A.3.

Fifthly, for some specific cells states below, the following method is used to calculate ∇c_p:

$$\nabla c_p(\vec{x}, t)_{\vec{r}} = \frac{-3c_p(\vec{x}, t) + 4c_p(\vec{x} + \vec{r}\Delta x, t) - c_p(\vec{x} + 2\vec{r}\Delta x, t)}{2\Delta x} + O(\Delta x^2) \tag{A.4}$$

in which $\vec{r}$ is a normalized direction vector. This method is used for the following cells:

- For cells whose neighbor in the $-\vec{r}$-direction is a model boundary or has a different phase, the component of ∇c_p in the $\vec{r}$-direction is calculated by eq. A.4

In all other cases, ∇c_p is calculated as

$$\nabla c_p(\vec{x}, t)_{\vec{r}} = \frac{c_p(\vec{x} + \vec{r}\Delta x, t) - c_p(\vec{x} - \vec{r}\Delta x, t)}{2\Delta x} + O(\Delta x^2) \tag{A.5}$$

in which $\vec{r}$ is a normalized direction vector.

A.2. Second Order Accurate algorithm

The difference between the first and second order accurate algorithm is that in the second order algorithm, equations A.1 and A.3 are not in use anymore. The components of ∇c_p that are calculated based on these equations are set to 0 in the second order accurate algorithm. This leads to the following algorithm.

First, some or all of the vector components of ∇c_p are set to 0 for the few cells for which ∇c_p is indeed 0 (first point below) or cannot be calculated (second, third and fourth point below). This is the case for the following cells:

- For cells in the mushy phase in case of a chemically pure substance, since $\nabla T = \vec{0}$ in this phase, $\nabla c_p = \vec{0}$

- For cells at the model boundary in the case that the neighboring cell opposite to the boundary or the cell behind this cell in the same direction is in a different phase, the component of ∇c_p perpendicular to the boundary should be set to 0

- For cells that are enclosed by two neighboring cells, on opposite sides with both a different phase to the enclosed cell, the component of ∇c_p in the direction of those two cells should be set to 0.

- For cells that are, together with one neighboring cell in the same phase, enclosed by two neighboring cells, on opposite sides with both a different phase to the enclosed cells, the component of ∇c_p in the direction of those two cells should be set to 0.

Secondly, for some specific cells states below, equation A.2 is used to calculate ∇c_p. This method is used for the following cells:

- For cells whose neighbor in the $\vec{r}$-direction is a model boundary or has a different phase, the component of ∇c_p in the $\vec{r}$-direction is calculated by eq. A.2

Thirdly, for some specific cells states below, equation A.4 is used to calculate ∇c_p. This method is used for the following cells:

- For cells whose neighbor in the $-\vec{r}$-direction is a model boundary or has a different phase, the component of ∇c_p in the $\vec{r}$-direction is calculated by eq. A.4

In all other cases, ∇c_p is calculated via A.5

B

Thermophysical Properties Data

B.1. Thermophysical Properties Water

B.1.1. Specific Heat c_p

For water, the following relations for c_p^ϕ (kJ/kg) were used, with temperature T in K:

Ice (solid) [9]:

$$c_p^s(T) = 0.185 + 0.689 \cdot 10^{-2}\, T \tag{B.1}$$

Water (liquid) [24]:

$$c_p^l(T) = 4.2174356 - 0.0056181625\,(T - 273.15) + 0.0012992528\,(T - 273.15)^{1.5}$$
$$- 0.00011535353\,(T - 273.15)^2 + 4.14964 \cdot 10^{-6} \cdot (T - 273.15)^{2.5} \tag{B.2}$$

The specific heat of the mushy zone is calculated by [6, 9, 24]:

$$c_p^m = \frac{2c_p^l(T) \cdot c_p^s(T)}{c_p^l(T) + c_p^s(T)} \tag{B.3}$$

For a temperature-dependent specific heat, $T = 273.15$ K is used, which leads to $c_p^m \approx 2773$ kJ/kgK

In the case of a temperature-independent specific heat ($c_p \neq c_p(T)$), if it is not denoted which temperature-independent values are used, the values

- $c_p^s(273.15K) \approx 2066$ kJ/kgK
- $c_p^l(273.15K) \approx 4217$ kJ/kgK

are used.

B.1.2. Thermal Conductivity λ

The value of the thermal conductivity λ in this thesis is obtained from [27]. Since in this source λ is discretely valued, a parabolic fit was performed on this data to accurately predict the thermal conductivity for local and lower temperatures. This leads to the following equations:

$$\lambda^s(T) = 9.508 - 0.04870T + (7.904 \cdot 10^{-5})T^2 \tag{B.4}$$

$$\lambda^l(T) = -0.7541 + 0.007434T - (9.674 \cdot 10^{-6})T^2 \tag{B.5}$$

$$\lambda^m(273.15K) = (1 - f_l)\lambda^s(273.15K) + f_l\lambda^l(273.15K) \tag{B.6}$$

These values are validated by Ratcliffe (1962) [25], since the values found are similar. If it is not explicitly stated that a variable or temperature-dependent thermal conductivity is used, temperature-independent

values of the thermal conductivity are used. For this temperature-independent thermal conductivity $(\lambda \neq \lambda(T))$, the values

- $\lambda^s(273.15K) = 2.10$ W/mK
- $\lambda^l(273.15K) = 0.55$ W/mK

are used.

B.1.3. Density ρ

The density of water in this thesis is taken to be single valued throughout space and time, at a value of $\rho_0 = 1000$ kg/m^3.

B.1.4. Latent Heat L

The latent heat L of water is valued at $L = 334$ kJ/kg [6].

B.2. Thermophysical Properties Paraffin

B.2.1. Specific Heat c_p

For paraffin, data from multiple studies [2, 4, 15, 17, 19, 22, 28] was recovered, as the studies showed significantly varying results. The data of the studies are illustrated in figure B.1. All studies except Jin and Wunderlich (1991) [17] showed a continuous function as a relation for the c_p. For Jin and Wunderlich, the specific heat c_p was given discrete. Between these discrete values, the c_p was interpolated. Of the studies, the average is established which is used for the numerical model of paraffin. For the solid specific heat, the results of the four studies by Ukrainczyk et al. (2010) [28], Kraiem et al. (2023) [19], Jin and Wunderlich (1991) [17] & Inaba and Tu (1997) [15] are averaged between 253 and 283 K and extrapolated from 283 K until the melting temperature T_m of 237 K. For the liquid specific heat, the results of all studies are averaged.
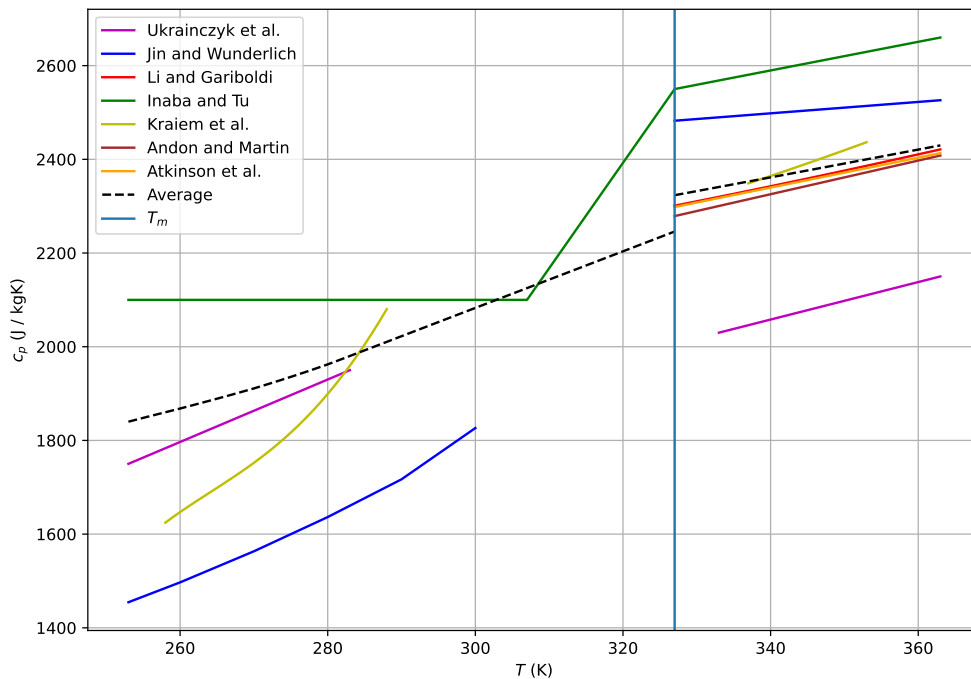

Figure B.1: Plot of the specific heat c_p of paraffin with a melting point of ~327 K found in various studies against temperature

B.2.2. Thermal Conductivity λ

The data of the thermal conductivity λ of paraffin was obtained by multiple studies. The thermal conductivity of solid paraffin λ^s was obtained by averaging Ukrainczyk et al. (2010) [28] and Inaba and Tu (1997) [15] to a value of $\lambda^s = 0.22$ W/mK. The thermal conductivity of liquid paraffin λ^l was obtained by Li and Gariboldi (2021) [22]:

$$\lambda^l = 0.2348 - 0.2056(\frac{T}{T_{boil}}) + 0.07128(\frac{T}{T_{boil}})^2 \tag{B.7}$$

with λ^l in W/mK, the temperature T and the boiling temperature T_{boil} in K and

$$T_{boil} = -201.366 + 6.341\, T_m - 0.02611\, T_m^2 + 4.56 \cdot 10^{-5}\, T_m^3 \tag{B.8}$$

with the melting temperature T_m in K. For $T_m = 327$ K, $T_{boil} = 674.66$ K. In the case it is not explicitly stated that a variable or temperature-dependent thermal conductivity is used, temperature-independent values of the thermal conductivity are used. In the case of a temperature-independent thermal conductivity ($\lambda \neq \lambda(T)$), the value $\lambda^l = 0.15$ W/mK is used.

The thermal conductivity of the mushy phase is calculated by $\lambda^m(T_m) = (1 - f_l)\lambda^s(T_m) + f_l\lambda^l(T_m)$.

B.2.3. Density ρ

The density of paraffin in this thesis is taken to be single valued throughout space and time, at a value of $\rho_0 = 800$ kg/m^3 [28].

B.2.4. Latent Heat L

The latent heat of paraffin L is obtained by averaging the results of Inaba and Tu (1997) [15], Kenisarin (2014) [18], Li and Gariboldi (2021) [22] and Ukrainczyk (2010) [28], which results in $L = 170$ kJ/kg.

C
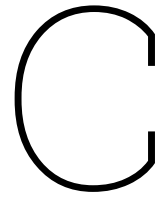
Experimental Data and Assumptions

C.1. Detailed list of materials
- Small 'enveloped' paraffin-filled cylindrical glass: inner / outer diameter: 14.40 / 15.80 mm, length 21.40 cm. Made of (Pyrex) glass.
- Large 'enveloping' cylindrical glass: inner / outer diameter: 25.40 / 27.50 mm, length 21.4 cm. Made of (Pyrex) glass.
- Hollow cylindrical copper heating element: outer diameter: 14.25 mm, length 31.05 mm.
- Wooden pieces for centering the enveloped glass inside the enveloping glass: inner / outer diameter: 15.80 / mm.
- Temperature-controlled hot water basin with hoses applied to the heating element. Temperature set: 363.55 K
- Paper tape measure, millimeter scale division, applied to the enveloped paraffin-filled glass with transparent adhesive tape
- Styrofoam, applied to the bottom of the enveloping glass to insulate the bottom of the enveloped glass from the bottom of the enveloping glass

C.2. Assumptions Heat Supply and Loss
In order to calculate the heat supply, Fourier's law (eq. 2.5) is used, multiplied by the area perpendicular to the heat flux of the material. The thermal conductivity $\lambda^l_{\text{paraffin}} = 0.15$ W/mK (App. B.2 and $\lambda_{\text{glass}} = 1.05$ W/mK [27] are assumed. $\nabla T = \frac{dT}{dx}$ is calculated by setting $dT = T_w - T_m = 36$ K and $dx = x_w - x_{fr}$ (the melting front propagation).

It was assumed that the glass had the same ∇T as the paraffin, which is a reasonable assumption if the thermal conductivities of the both are compared. The effective thermal conductivity $\lambda^l_{eff,\,\text{paraffin}}$ is a combination of the two, by incorporating the heat flux through the glass in the heat flux through the paraffin, as if all heat was conducted through the paraffin and none through the glass. It is calculated by

$$\lambda^{s/l}_{eff,\,\text{paraffin}} = \frac{\lambda^{s/l}_{\text{paraffin}} A_{\text{paraffin}} + \lambda^{s/l}_{\text{glass}} A_{\text{glass}}}{A_{\text{paraffin}}} \tag{C.1}$$

with $A_{\text{paraffin / glass}}$ the area of the paraffin / glass.

In order to calculate the heat loss, two sources are considered: heat diffusion and radiation. It was assumed that only heat was lost on the outer, enveloped glass side around the liquid paraffin. Therefore, the area through which heat is lost is calculated by

$$A_{loss} = (x_w - x_{fr})\pi D_{\text{out, enveloped glass}} \tag{C.2}$$

The heat diffusion is again calculated by Fourier's law (eq. 2.5). The thermal conductivity $\lambda_{\text{air}} = 0.024$ [27] was taken. The temperature of the outside of the enveloping glass was measured in (almost) steady state (after 4 hours of experiment) at 309.15 K. By assuming the outer temperature of the enveloped glass to be 333.15 K, this leads to the following inner diameter temperature of the enveloping glass $T_{\text{g,in}}$ if a steady state is assumed:

$$q''_{\text{glass}} = q''_{\text{air}} \tag{C.3}$$

$$\lambda_{\text{glass}} \frac{309.15 - T_{\text{g,in}}}{0.0021} = \lambda_{\text{air}} \frac{T_{\text{g,in}} - 333.15}{0.0048} \tag{C.4}$$

which leads to $T_{\text{g,in}} \approx 309.4$ K.

The heat radiation was calculated using Stefan-Boltzmann's law

$$q''_{rad} = \epsilon_{eff} \sigma (T_1^4 - T_0^4) \tag{C.5}$$

with T_1 in this case being the temperature of the outer layer of the enveloped glass (assumed at 333.15 K) and T_0 the temperature of the inner layer of the enveloping glass (calculated at 309.4 K). ϵ_{eff} is the effective emissivity and is calculated by

$$\epsilon_{eff} = \left(\frac{1}{\epsilon_{\text{glass}}} + \frac{D_1}{D_0} \frac{1 - \epsilon_{\text{glass}}}{\epsilon_{\text{glass}}} \right)^{-1} \tag{C.6}$$

with $\epsilon_{\text{glass}} = 0.80$ [27], and D_1 in this case being the diameter of the outer layer of the enveloped glass and D_0 the diameter of the inner layer of the enveloping glass. This leads to $\epsilon_{eff} \approx 0.71$

C.3. Derivation Hot Water Temperature Decrease in Heating Element

Similar to section C.2, in order to calculate the heat supply from the heating element to the paraffin, Fourier's law (eq. 2.5) is used, multiplied by the area perpendicular to the heat flux of the material.

The thermal conductivity $\lambda^l_{\text{paraffin}} = 0.15$ W/mK (App. B.2) is assumed. $\nabla T = \frac{dT}{dx}$ is calculated by setting $dT = T_w - T_m = 36$ K and $dx = x_w - x_{fr}$ (the melting front propagation). For the area, the contact area with the paraffin is assumed, based on the inner diameter of the enveloped glass.

This leads to a heat influx in the paraffin of

$$q''_{\text{in}} = \frac{0.8794}{x_{fr}} \tag{C.7}$$

with x_{fr} in mm. The temperature decrease ΔT of the hot water is equal to

$$\Delta T = \frac{q''_{\text{in}}}{FR \cdot \rho c_p} = \frac{q''_{\text{in}}}{42.2} \tag{C.8}$$

with ΔT the decrease in the temperature (K), ρ the density (kg/L), c_p the specific heat (J/kgK) and FR the flowrate (L/s), which is assumed to be 10 mL/s.

Combining these equations results in

$$\Delta T = \frac{0.8794}{42.2 \cdot x_{fr}} = \frac{0.021}{x_{fr}} \tag{C.9}$$

which show that the temperature decrease in the water is lower than 0.5 K for the melting front exceeding 0.04 mm, which is almost instantly.

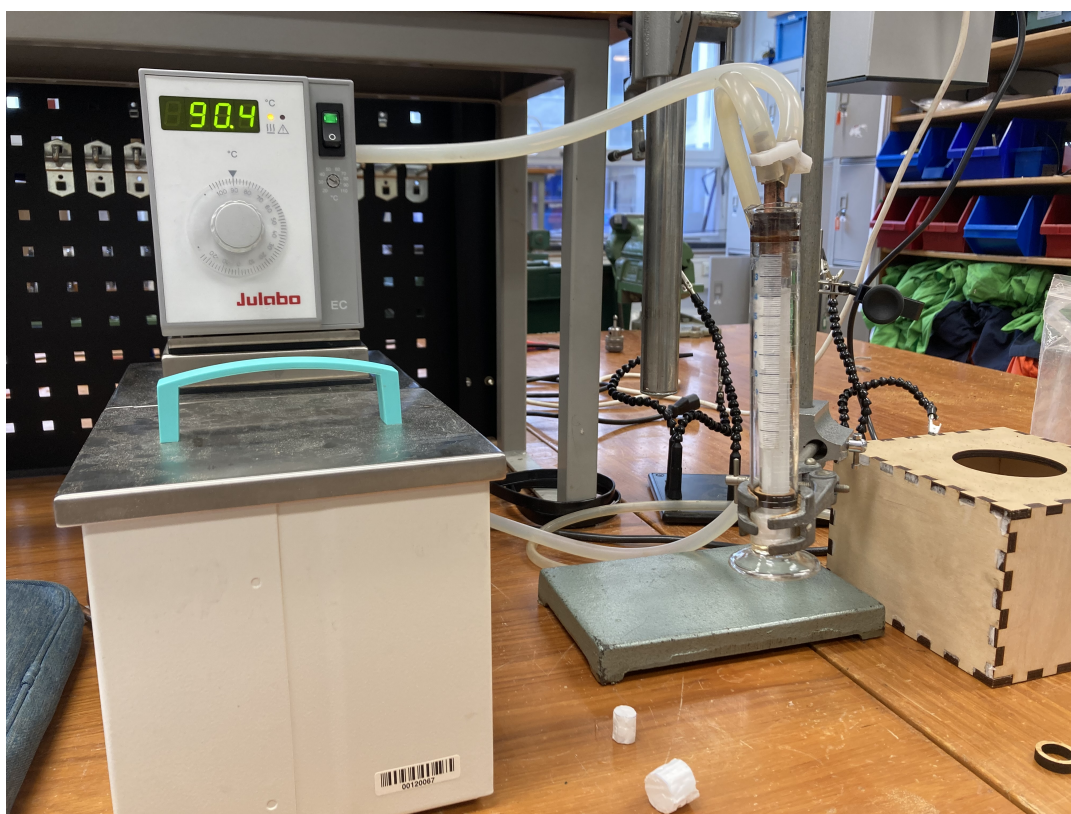## C.4. Picture of the Experimental Setup

Figure C.1: Picture of the experimental setup

Derivation of Enthalpic Balance Equation for Temperature-Dependent Specific Heat

$$\nabla \cdot (a_v^\phi \nabla h_v^\phi) = \nabla a_v^\phi \cdot \nabla h_v^\phi + a_v^\phi \nabla^2 h_v^\phi \tag{D.1}$$

$$= (\frac{\lambda^\phi}{\rho}(\frac{d\frac{1}{c_{p,v}}}{dT})\nabla T) \cdot (T\frac{dc_{p,v}^\phi}{dT}\nabla T + c_{p,v}\nabla T) + a_v^\phi \nabla \cdot (T\frac{dc_{p,v}^\phi}{dT}\nabla T + c_{p,v}\nabla T) \tag{D.2}$$

$$= (\frac{\lambda^\phi}{\rho}(-\frac{1}{c_{p,v}^{\phi\,2}})(\frac{dc_{p,v}^\phi}{dT})\nabla T) \cdot (T\frac{dc_{p,v}^\phi}{dT}\nabla T + c_{p,v}\nabla T)$$

$$+ a_v^\phi(\nabla T \cdot \frac{dc_{p,v}^\phi}{dT}\nabla T + \nabla(\frac{dc_{p,v}^\phi}{dT}) \cdot T\nabla T + T\frac{dc_{p,v}^\phi}{dT}\nabla^2 T + \nabla c_{p,v} \cdot \nabla T + c_{p,v}\nabla^2 T) \tag{D.3}$$

$$= -\frac{a_v^\phi T}{c_{p,v}^\phi}(\frac{dc_{p,v}^\phi}{dT})^2|\nabla T|^2 - a_v^\phi(\frac{dc_{p,v}^\phi}{dT})|\nabla T|^2$$

$$+ a_v^\phi(\frac{dc_{p,v}^\phi}{dT})|\nabla T|^2 + a_v^\phi \nabla(\frac{dc_{p,v}^\phi}{dT}) \cdot T\nabla T + a_v^\phi T(\frac{dc_{p,v}^\phi}{dT})\nabla^2 T + a_v^\phi(\frac{dc_{p,v}^\phi}{dT})|\nabla T|^2 + a_v^\phi c_{p,v}^\phi \nabla^2 T \tag{D.4}$$

$$= a_v^\phi T\nabla(\frac{dc_{p,v}^\phi}{dT}) \cdot \nabla T + a_v^\phi(\frac{dc_{p,v}^\phi}{dT} - \frac{T}{c_{p,v}^\phi}(\frac{dc_{p,v}^\phi}{dT})^2)|\nabla T|^2 + a_v^\phi(T\frac{dc_{p,v}^\phi}{dT} + c_{p,v}^\phi)\nabla^2 T \tag{D.5}$$

E

Julia Code

The Julia code used in this thesis can be found in this hyperlink:
Google Drive